RESEARCH ARTICLE

Coupled Lateral and Longitudinal Controller for Over-Actuated Vehicle in Evasive Maneuvering With Sliding Mode Control Strategy

AMAURI DA SILVA JUNIOR[1,2]**, CHRISTIAN BIRKNER**[1]**, REZA NAKHAIE JAZAR**[2]**,
AND HORMOZ MARZBANI**[2]

[1]Technische Hochschule Ingolstadt, 85049 Ingolstadt, Germany
[2]School of Engineering, Royal Melbourne Institute of Technology, RMIT University, Melbourne, VIC 3083, Australia

Corresponding author: Amauri da Silva Junior (amauri.dasilvajunior@thi.de)

ABSTRACT Coupled controllers are vital for safely handling vehicles, especially in critical driving situations that include changing lanes to avoid obstacles. Controllers specialized in emergencies must keep road users safe in critical situations. In this paper, we develop the coupled controller to handle evasive maneuvers for an over-actuated vehicle. The controller is based on the second-order sliding mode control theory. We use the bicycle model to establish the equivalent and robust steering equations as a control-oriented model. The lateral and longitudinal vehicle motions are coupled to each other by the lateral vehicle information on the longitudinal sliding surface, and the dependence of the lateral sliding surface on the longitudinal velocity. The torque vectoring method based on fuzzy logic adjusts the yaw moment. We address the tire slip circle on the slip controller to stabilize the vehicle while maneuvering. We simulate and evaluate our controller in a rear-end collision situation with a short time window to maneuver the vehicle. The ego vehicle detects the preceding vehicle and performs an evasive lane change while simultaneously applying brakes to bring the vehicle to a halt. Our research is the earliest in providing an ultimate emergency control to successfully avoid crashes up to 130 km/h in short time crash detection.

INDEX TERMS Autonomous vehicle, crash avoidance, evasive maneuvers, over-actuated vehicle, sliding mode control, vehicle coupled controllers.

I. INTRODUCTION

Autonomous vehicles (AVs) are expected to dominate the roads by 2050 [1]. AVs aims to reduce road accidents and traffic fatalities to zero [2]. Therefore, AVs must be able to handle the vehicle in every situation, including emergencies, and keep road users safe. In an emergency, the vehicle's active safety system must control the car up to the tire saturation limits while keeping the car in a stable condition, i.e., there is no loss of control while attempting to avoid a crash [3]. Active vehicle safety systems may consist of longitudinal, lateral, or coupled functions.

State-of-the-art longitudinal functions include adaptive cruise control (ACC), cooperative adaptive cruise control (CACC), and automated emergency braking (AEB) [4]. In detail, ACC automatically controls the throttle and brake pedals to keep the vehicle velocity constant while maintaining a safe distance from preceding vehicles. CACC is an extension of ACC, which includes vehicle-to-vehicle (V2V) and infrastructure-to-vehicle (I2V) communication [5]. AEB is an active safety function that attempts to avoid crashes by autonomously applying brakes if a critical situation arises [6].

Lateral functions are designed to track the reference path and determine the optimal steering angles while maintaining vehicle stability. State-of-the-art systems available on the market include lane keep assistant (LKA), lane centering

The associate editor coordinating the review of this manuscript and approving it for publication was Guillermo Valencia-Palomo.

(LC), emergency steering assist (ESA), and autonomous emergency steering (AES). LKA and LC systems support the driver by retaining the vehicle between the lane marks. Whereas LKA operates only when the vehicle is close to the lane edges, LC is a constant active steering system [7]. ESA is an active safety function that supports the driver in emergency steering, but the driver has to self-initiate the maneuver [8]. The AES system automatically performs an evasive steering maneuver when an imminent collision is detected [9].

Control methods such as homogeneous domination control and sampled-data control have been developed for vehicle applications, especially for the design of lateral controllers. Homogeneous domination control was proposed in [10]. The method can be applied to linear and non-linear systems and does not require a strict linear growth condition, as for global output feedback stabilization [10], [11]. In [12], a lane-keeping control method with a homogeneous domination approach was presented with stability proved via the Lyapunov method. The controller was evaluated in a simulation environment and via a driverless test vehicle up to 80 km/h, with a maximum of 0.06 meters deviation from the desired path. Sampled-data controllers for lateral motion considering uncertain disturbances for velocities up to 80 km/h were proposed in [13], [14], [15]. The mentioned controllers in [11], [12], [13], [14], and [15] were not investigated for evasive maneuvers, coupled lateral and longitudinal motion, nor at the vehicle handling limits. In [16], an evasive steering assist was proposed for velocities up to 90 km/h, distance to maneuver of 50 meters and time-to-collision of 2.4 seconds.

Vehicle active safety functions for coupled lateral and longitudinal functions are challenging control types because they deal with coupling the nonlinear forces in longitudinal and lateral directions [17]. Key solutions for coupled controls include model predictive control (MPC), machine learning algorithms, and sliding mode control (SMC) [18], [19], [20], [21], [22], [23], [24], [25], [26], [27]. In these solutions, however, there exist many restrictions. In [19], the vehicle avoided crashes up to 100 km/h, and the controller cannot be safely applied beyond it. The controller in [20] prioritized collision avoidance, vehicle stability, and path tracking over passenger comfort. However, the controller was only investigated and avoided crashes for velocities up to 40 km/h. The SMC controller in [21] handled the coupled lateral and longitudinal motion up to 36 km/h in double lane-change, but it did not consider critical scenarios. The MPC controller developed in [24] was designed for urban environments and therefore was evaluated for a maximum velocity of 40 km/h, lateral accelerations up to 1.5 m/s², and longitudinal accelerations up to 2 m/s², which are within the range of normal driving conditions [28].

SMC is a robust control due to its insensitivity to system uncertainties. It presents a fast response and robustness to external disturbances [29]. The main SMC methods applied in engineering applications are the first and higher-order approaches (mainly second and third-order). The first-order approach drives the sliding surface to zero, whereas the
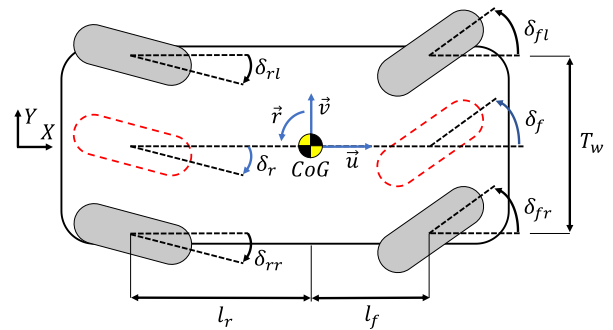

FIGURE 1. Schematic diagram of the 4WIS-4WID-4WIB vehicle and the simplified single-track bycicle model in red dashed lines.

second-order drives both the sliding surface and its derivative in finite time to zero. The third-order additionally drives the second derivative of the sliding surface to zero [30], [31]. The SMC's first-order main disadvantage is the high-frequency oscillations near the sliding surface, known as the chattering effect. The chattering effect attenuation is commonly done by using higher-order sliding theory. Therefore, higher-order is the most common type for vehicle controllers that use SMC theory, as in [21], [26], and [32]. Other recent SMC strategies include fractional-order [27], [33], [34] and the use of machine learning combined with SMC [25], [35], [36], [37]. Whereas MPC can accommodate vehicle non-linearities and multiple hard and soft constraints, its main disadvantage is the high computational cost, which can be unsuitable for real-time applications [38]. The computational time for SMC and MPC controllers was investigated in [39], with SMC performing four times faster than the MPC controller.

Whereas all of the mentioned studies focused on front-wheel steering, car manufacturers and researchers have also investigated and proposed prototypes for future over-actuated vehicles, which have more actuators than degrees-of-freedom to be controlled [40], [41], e.g., four-wheel steering, four-wheel drive, and four-wheel brake (4WS-4WD-4WB), or four-wheel independent steering, four-wheel independent drive, and four-wheel independent brake (4WIS-4WID-4WIB), as shown in Figure 1. Both configurations offer enhanced vehicle stability and maneuverability over the active front steering (AFS) and front-wheel independent steering (FWIS) [42]. The different steering configurations are defined based on the correlation between the steering angle of each wheel, as [42]

$$
\begin{aligned}
\text{AFS:} \quad & \delta_{fl} = \delta_{fr}, \ (\delta_{rl} = \delta_{rr} = 0), \\
\text{FWIS:} \quad & \delta_{fl}, \ \delta_{fr}, \ (\delta_{rl} = \delta_{rr} = 0), \\
\text{4WS:} \quad & \delta_{fl} = \delta_{fr}, \ \delta_{rl} = \delta_{rr}, \\
\text{4WIS:} \quad & \delta_{fl}, \ \delta_{fr}, \ \delta_{rl}, \ \delta_{rr},
\end{aligned}
\tag{1}
$$

where δ_j is the individual steering values on each wheel ($j = fl, fr, rl, rr$). Whereas in 4WS the front and rear wheels turn in parallel, in 4WIS each wheel can turn with different
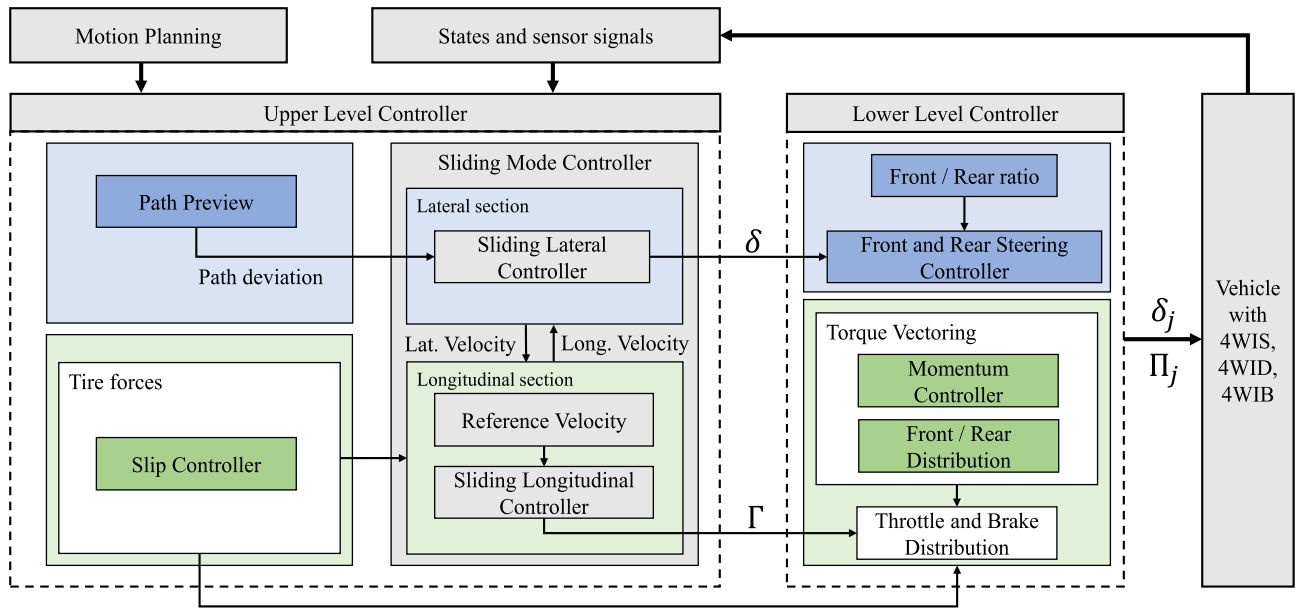
FIGURE 2. Control system architecture with upper and lower levels controllers.

steering angles from each other. The authors in [43] proposed a non-smooth finite time controller for a vehicle with 4WS and 4WD. The controller was evaluated in Carsim for a double lane-change maneuver for velocities up to 90 km/h. The proposed controller in [43] has shown better tracking accuracy than an SMC controller. However, neither the proposed controller nor the SMC controller was designed for evasive maneuvers but for normal driving situations. The study in [44] proposed an integrated control for evasive cases integrating various vehicle subsystems for a 4WIS-4WID-4WIB configuration. However, improvements on the 4WIS-4WID-4WIB studies are essential to solve emergency application restrictions.

This work presents a coupled lateral and longitudinal controller based on a second-order sliding mode control for emergencies for 4WIS-4WID-4WIB vehicles with fuzzy-based slip control and torque vectoring control. We propose a complete system architecture with an upper and lower-level controller, as shown in Figure 2. The SMC control part is responsible for coupling the lateral movement in terms of the steering angle as a function of longitudinal parameters, and the longitudinal movement in terms of the throttle and brake pedal as a function of lateral parameters.

The sensor signals are passed to the upper-level controller, including a virtual inertial measurement unit and a radar for object detection. The motion planning determines the reference path to be followed by the ego vehicle and passes it to the upper-level controller. On the upper level, the path preview algorithm determines the path deviation based on look-ahead areas. The SMC lateral and longitudinal functions define the vehicle steering angle δ and the desired throttle and brake pedal position Γ. SMC functions are coupled. The coupling between lateral and longitudinal movements can be

guaranteed by making the lateral sliding surface dependent on the vehicle yaw rate and consequently on the longitudinal vehicle velocity, and by making the longitudinal sliding surface dependent on the lateral path error, as in [21]. Therefore, by the coupling strategy, the requests on the steering are influenced by the brake and throttle pedals, whereas the vehicle's lateral movement influences the throttle and brake requests.

A sliding surface is generated for the lateral motion with three parameters: the lateral path error, the lateral velocity error, and the yaw rate error. A sliding surface for the longitudinal movement is developed with four parameters: the distance between the ego vehicle and the preceding vehicle, the relative longitudinal velocity, the lateral path error, and the tire slip information. Lateral and longitudinal sliding equations are described in sections II-B and II-E. The fuzzy-based slip control calculates the correction for the throttle and brake torques, so the tire forces on the wheels keep within or close to saturation limits. On the lower level controller, the torque vectoring based on fuzzy logic corrects the torque request independently on each wheel and delivers the individual throttle and brake values Π_j. The front and rear steering ratios are calculated and passed as an input for the steering controller, which then determines the individual steering values on each wheel δ_j.

We test our controller on a high-fidelity vehicle simulator for a 4WIS-4WID-4WIB vehicle. The controller's primary purpose is to perform emergency steering combined with emergency braking, bringing the vehicle to its handling limits. The main scenario for validation is a single-lane change. The controller is also evaluated for different road frictions. We test the controller for velocities up to 130 km/h, as it is the maximum recommended velocity for autonomous vehicles on highways and because most countries' velocity limits are

equal to or below it [45]. The proceeding object is detected within 30 meters of a crash (or 830 milliseconds when the ego vehicle drives at 130 km/h). Compared to previous studies, the main research contributions of this paper are:

- a controller specialized for emergency maneuvers to handle the vehicle up to handling limits including a coupled lateral and longitudinal motion via SMC theory for 4WIS-4WID-4WIB vehicles.
- novel sliding surfaces for both lateral and longitudinal motion including a coupling strategy via the use of lateral parameters on the longitudinal surface and the dependency of longitudinal parameters on the lateral surface.
- a novel controller architecture using SMC theory on the upper level controller together with individual slip controller, torque-vectoring strategy, and path preview technique.
- the design of a novel path preview technique based on look-ahead areas and not only on look-ahead points as generally used in literature.

This paper is organized as follows: Section II presents the design of our vehicle controller, along with the proposed system architecture, vehicle modeling, path planning strategy, and the designs of the torque vectoring and the slip control. The vehicle characteristics and simulation software are provided in Section III. Section IV devotes the test scenarios and performance indicators. The result description is given in Section V, and conclusions in Section VI.

II. VEHICLE CONTROLLER DESIGN

Sliding mode control is one of the most efficient robust control strategies and one of the principal approaches to controlling uncertain systems, including insensitivity to perturbations [46]. The central concept of SMC is to choose one sliding variable σ as follows

$$\sigma = x_1 + cx_2, \tag{2}$$

in which, x_1 and x_2 are the state variables of interest, and c is the gradient coefficient. The sliding variable σ is forced in a finite time t_r to $\sigma \equiv 0$ and $\dot{\sigma} \equiv 0$, meaning that the state variables x_1 and x_2 asymptotic converge to zero with a given convergence ratio. Once the sliding variable σ becomes zero, it establishes the sliding surface. The sliding surface is reachable if $\sigma\dot{\sigma} < 0$. The convergence of the state variables is only possible by designing a control $\eta = \eta(x_1, x_1)$ that is capable of holding $\sigma(t, x_1, x_2) = 0$. Every time a deviation from $\sigma = 0$ is detected, the control η must apply sufficient effort to maintain the state variables on the sliding surface. This effort results in a high-frequency switching of control, producing undesired system oscillations called the chattering effect [46], [47], [48]. The three main elimination and mitigation techniques for chattering include: the use of smooth functions instead of discontinuous ones, the use of an observed-based approach, and the higher-order sliding mode approach (HOSMs) [49]. Smooth functions only guarantee

convergence to a boundary layer around the sliding surface. The observer approach reduces chattering but deteriorates robustness. HOSMs can force not only the sliding variables to zero on finite time but also the (k-1) successive derivatives, with k the order of the sliding mode [47]. In this work, we use the higher-order super-twisting approach to ensure robust stability and chattering mitigation. The sliding mode controller η is written as [50], [51], and [52]

$$\eta = \eta_e + \eta_r, \tag{3}$$

where η_e and η_r are equivalent and robust parts, respectively. The equivalent part η_e refers to the control law that makes the state variables remain on the sliding surface. It is calculated considering $\dot{\sigma} = 0$. Therefore, η_e ensures that the system will always remain on the sliding surface once it is reached. The robustness control η_r is designed based on the super-twisting approach. Super-twisting approach is a continuous second-order sliding mode control based on the Lyapunov stability theorem. It can converge in finite time, have superior chattering attenuation over classical sliding mode methods, and are suitable for real-time applications. Super-twisting control handles the uncertainties and disturbances while forcing the system towards the sliding surface and ensuring the system's convergence so that $\sigma\dot{\sigma} < 0$. It is named second-order because it drives both σ and $\dot{\sigma}$ to zero in finite time [21], [47], [50], [53], [54].

A. VEHICLE DYNAMICS MODELING

The lateral control development for the 4WIS-4WID-4WIB vehicle is based on a non-linear single-track bicycle model with independent front and rear-wheel steering, as shown in Figure 1. The simplified vehicle model allows for a straight-forwarding design of the steering angle equations, and it is a common practice for over-actuated vehicles, as in [55] ans [56]. The state-space equations of vehicle dynamics are written as

$$\begin{bmatrix} \dot{v} \\ \dot{r} \end{bmatrix} = A \begin{bmatrix} v \\ r \end{bmatrix} + B \begin{bmatrix} \delta_f \\ \delta_r \end{bmatrix}, \tag{4}$$

$$A = \begin{bmatrix} a_{11} & a_{12} \\ a_{21} & a_{22} \end{bmatrix} = \begin{bmatrix} -\dfrac{C_f + C_r}{m_v u} & -u - \dfrac{l_f C_f - l_r C_r}{m_v u} \\ -\dfrac{l_f C_f - l_r C_r}{I_z u} & -\dfrac{l_f^2 C_f + l_r^2 C_r}{I_z u} \end{bmatrix}, \tag{5}$$

$$B = \begin{bmatrix} b_{11} & b_{12} \\ b_{21} & b_{22} \end{bmatrix} = \begin{bmatrix} \dfrac{C_f}{m_v} & \dfrac{C_r}{m_v} \\ \dfrac{l_f C_f}{I_z} & -\dfrac{l_r C_r}{I_z} \end{bmatrix}, \tag{6}$$

in which v and r are respectively the lateral and yaw velocity of the vehicle's center of gravity (CoG); l_r and l_f are the distance from CoG to the rear and frontal axles; m_v is the total mass of the vehicle, including sprung and unsprung masses; u is the longitudinal velocity on the vehicle coordinate system xoy; r is the yaw rate. Assuming Ackerman steering geometry, the steering angle of each independent wheel is calculated

as [56]

$$\tan \delta_{fl} = \frac{\tan \delta_f}{1 - F_r}, \quad \tan \delta_{fr} = \frac{\tan \delta_f}{1 + F_r},$$

$$\tan \delta_{rl} = \frac{\tan \delta_r}{1 - F_r}, \quad \tan \delta_{rr} = \frac{\tan \delta_r}{1 + F_r}, \quad (7)$$

$$F_r = \frac{T_w}{2L}(\tan \delta_f - \tan \delta_r), \quad (8)$$

in which T_w is the track width.

A mathematical equation to calculate the rear-steering was developed in [57] as a function of the front steering, longitudinal velocity, vehicle, and tire characteristics. The concept relies on adjusting the rear steering to keep the vehicle centerline tangential to the curvature in all velocity ranges, as shown in Figure 3. The ratio of the front steering angle δ_f to the rear steering δ_r is written as [57]

$$k = \frac{\delta_r}{\delta_f} = -\frac{l_r - u^2 \frac{m_v l_f}{C_r L}}{l_f + u^2 \frac{m_v l_r}{C_f L}}, \quad (9)$$

with I_z the yaw moment of inertia. L the vehicle wheelbase, and C_f and C_r are the cornering stiffness of the front and rear tires, with $C_f = C_{fl} + C_{fr}$ and $C_r = C_{rl} + C_{rr}$. As the controller is designed to handle the vehicle in evasive maneuver, the model has to consider tire nonlinearities. We model the tire dynamics via the full tire magic formula from Pacejka [58]. Therefore, the cornering stiffness of each individual tire (C_{fl}, C_{fr}, C_{rl}, C_{rr}) do not receive a fixed value, but they are calculated from the tire magic formula.

B. LATERAL CONTROL BASED ON SMC
In this section the lateral control to define the vehicle steering angle is described. First, we define the sliding variable σ in the following form

$$\sigma = k_{yd} \Delta y + k_{yv} \Delta \dot{y} + k_r \Delta r, \quad (10)$$

in which Δy is the distance between the vehicle's CoG and the reference path in the perpendicular direction Y of the vehicle coordinate system (see Figure 3); $\Delta \dot{y}$ is the relative lateral velocity between CoG and the reference path; k_{yd}, k_{yv}, $k_r \in \mathbb{R}$ [59] are the gradient coefficients that can be adjusted as a function of state and time respectively. Δr is the difference between the actual and desired yaw rate r_d. Considering that the vehicle follows the path tangentially. r_d is derived in terms of longitudinal velocity, vehicle characteristics, tire characteristics, and steering angle [60].

$$r_d = \Phi \delta, \quad \text{with} \quad \Phi = \frac{u}{l_r + l_f + \frac{m_v}{l}(\frac{l_r}{C_f} - \frac{l_f}{C_r})u^2}. \quad (11)$$

The control η is rewritten as the steering angle δ as

$$\delta = \delta_e + \delta_{rb}, \quad (12)$$

where δ_e and δ_{rb} are the equivalent and robustness parts. By assuming $\delta = \delta_f$, the steering angles for each wheel can be then determined using (7).
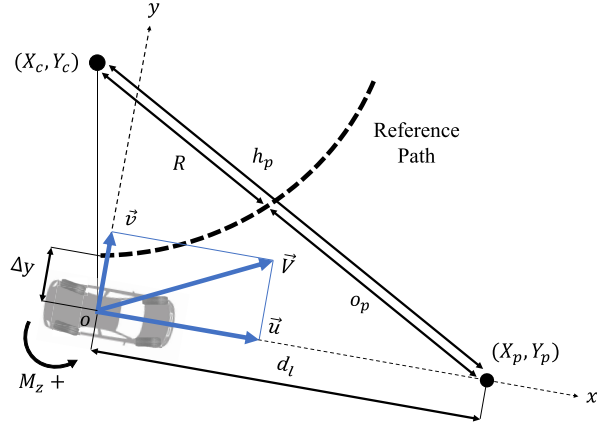

FIGURE 3. Vehicle driving tangentially to circular reference path, and look-ahead projection distant by d_l from vehicle.

1) EQUIVALENT PART DESIGN (δ_e)
The design of the equivalent part of the steering angle is defined in a three-step process. First, the lateral vehicle velocity is derived from the sliding variable σ, and later by conidering the vehicle following the path tangentially in a circular motion as shown in Figure 3. Finally, both equations for lateral velocity are combined to define the equivalent steering angle.

- Lateral velocity based on the sliding variable σ:
  Considering that the state variables have reached the sliding surface with $\sigma = 0$ and $\dot{\sigma} = 0$, the controller is capable of keeping the state variables ($\Delta y, \Delta \dot{y}, \Delta r$), on the sliding surface for $t > t_i$, with t_i the time the sliding surface is reached [47]. $\dot{\sigma}$ is written as

$$\dot{\sigma} = k_{yd} \Delta \dot{y} + k_{yv} \Delta \ddot{y} + k_r \Delta \dot{r} = 0, \quad (13)$$

here, $\Delta \ddot{y}$ is the relative lateral acceleration between CoG and the reference path written as

$$\Delta \ddot{y} = \ddot{y} - \ddot{y}_{ref}, \quad (14)$$

with lateral acceleration $\ddot{y}$ and the lateral acceleration reference $\ddot{y}_{ref}$ defined as [51]

$$\ddot{y} = \dot{v} + ru, \quad \ddot{y}_{ref} = u^2/R, \quad (15)$$

where R the curvature radius. The difference between vehicle and path velocity $\Delta \dot{y}$ yields

$$\Delta \dot{y} = v - v_{ref}, \quad (16)$$

with v_{ref} defined by considering the vehicle in quasi-steady-state circular motion, and in terms of curvature radius R, desired yaw rate r_d and longitudinal velocity u as [61]

$$v_{ref} = \begin{cases} \sqrt{(r_d R)^2 - u^2} & \text{, if } |R| < \infty \\ 0 & \text{, if } R = \infty \end{cases}. \quad (17)$$

A combination of (13) and (16) provides the vehicle lateral velocity v

$$v = -\frac{k_{yv}\Delta\ddot{y}}{k_{yd}} - \frac{k_r\Delta\dot{r}}{k_{yd}} + v_{ref}. \quad (18)$$

- Lateral velocity based on circular motion [61]:
Consider the vehicle in a quasi-steady-state (QSS) motion on a circular path with the vehicle centerline tangential to the curvature, as shown in Figure 3. QSS approximations have been widely applied in vehicle controllers up to handling limits [62], [63], [64]. The QSS approximation assumes that the track can be split into segments. It is valid if the vehicle's states change slowly between path segments, which is achieved by making the path segments small [64]. Therefore, given that the changes in lateral and longitudinal motion change slowly in each small path segment, the QSS approach yields the assumption that the vehicle behaves as in a steady motion in each segment, and thus the term *quasi* [65]. Thus, the yaw and lateral accelerations ($\dot{r}$, $\dot{v}$) can be neglected for each independent segment [62]. According to the study in [66], the main difference between the steady-state (SS) approach and QSS is that, in SS, the lateral and longitudinal motions are modeled separately, whereas QSS considers both motions coupled. As in the current study, the SMC controller for lateral and longitudinal motion are coupled via the sliding variables, and QSS is a common approach in literature for controllers up to handling limits, we assume the QSS hypothesis. Moreover, according to [67], QSS is a valid assumption for vehicle controllers with a path following strategy. The path following strategy of this study is described in section II-C. SMC with QSS assumptions has been designed for, e.g., vehicle and electronic systems in [68], [69], and [70]. Therefore, let's consider the vehicle driving in a path segment in the QSS condition ($\dot{v} = \dot{r} = 0$). Equation (4) becomes

$$-A\begin{bmatrix} v_{qss} \\ r_{qss} \end{bmatrix} = B\begin{bmatrix} 1 \\ k \end{bmatrix}\delta_{qss}, \quad (19)$$

and the vehicle lateral velocity in quasi steady-state v_{qss} is calculated as a function of the yaw rate r_{qss} as [61]

$$v_{qss} = r_{qss}T, \quad (20)$$

in which,

$$T = -\frac{a_{12}(b_{21} + b_{22}k) - a_{22}(b_{11} + b_{12}k)}{a_{11}(b_{21} + b_{22}k) - a_{21}(b_{11} + b_{12}k)}. \quad (21)$$

The vehicle velocity V in tangential motion relative to the path can be written as a function of the lateral velocity v, the longitudinal velocity u, and equal to the product of the yaw rate r and the curvature radius R as

$$V_{qss} = \sqrt{u^2 + v_{qss}^2} = r_{qss}R. \quad (22)$$

Combining (20) and (22), we obtain the expression of the yaw rate being a function of R and T as

$$r_{qss} = \frac{u}{\sqrt{R^2 - T^2}}. \quad (23)$$

Here, we assume that the longitudinal velocity u is constant, the vehicle follows the reference path, and the error between reference and actual paths is much smaller than the curvature radius, i.e. $\Delta y \ll R$. By using (19) to (21), we obtain the vehicle steering angle δ_{ss} in the following form

$$\delta_{qss} = \frac{P}{\sqrt{R^2 - T^2}}, \quad (24)$$

with

$$P = L + \frac{u^2m_v(l_fC_f - l_rC_R)}{lC_fC_R}. \quad (25)$$

The look-ahead offset o_p is the distance between the look-ahead point (X_p, Y_p) and the reference path. h_p is the distance between the center of curvature (X_c, Y_c) and the look-ahead point, written as

$$o_p = h_p - R, \quad (26)$$

with

$$h_p = \sqrt{R^2 + d_l^2 + 2Rd_l(-v_{qss})/V}. \quad (27)$$

Using (20), (22), (26), we obtain the final expression for the look-ahead offset as

$$o_p = \sqrt{R^2 + d_l^2 + 2d_lT} - R. \quad (28)$$

By using the Taylor's expansion

$$\forall x, \varepsilon \in \mathbb{R}, x > 0, \frac{|\varepsilon|}{x} \ll 1 \rightarrow \sqrt{x + \varepsilon} = \sqrt{x} + \frac{\varepsilon}{2\sqrt{x}}, \quad (29)$$

and assuming that $d_l|(1 + 2T)|/R \ll 1$, $|T|/R \ll 1$, and thus $1 - T^2/R^2 = 1$, a combination of (24) and (28) gives the ratio between steering angle and look-ahead offset

$$\frac{\delta_{qss}}{o_p} = \frac{2P}{d_l(d_l + 2T)}. \quad (30)$$

Substituting (20) into (30), we obtain the lateral velocity in steady-state v_{qss}

$$v_{qss} = \left[\frac{2o_pP}{d_l\delta_{qss}} - d_l\right]\frac{r_{qss}}{2}. \quad (31)$$

- Equivalent steering angle (δ_e):
By assuming QSS approach, let's consider $v_{qss} = v$, $r_{qss} = r$, and $\delta_e = \delta_{qss}$. The steering angle equivalent equation is derived from (18) and (31) as

$$\left[\frac{2o_pP}{d_l\delta_e} - d_l\right]\frac{r}{2} = -\frac{k_{yv}\Delta\ddot{y}}{k_{yd}} - \frac{k_r\Delta\dot{r}}{k_{yd}} + v_{ref}. \quad (32)$$

We assume that the vehicle can follow the track with a good accuracy, i.e. $v_{ref}/r \approx T$. Substituting r by (23),

and considering $\sqrt{R^2 - T^2} = P/\delta_{qss}$ as in (24), the equivalent steering equation is thus rewritten as

$$\delta_e = \frac{2P}{d_l(d_l + 2T)}\left[o_p + \frac{k_{yv}\Delta\ddot{y}d_l}{k_{yd}u} + \frac{k_r\Delta\dot{r}d_l}{k_{yd}u}\right]. \quad (33)$$

2) ROBUSTNESS PART (δ_{rb})

The robustness part of the steering angle equation δ_{rb} is derived from the second-order super-twisting control strategy, and it is written in the following form [47]:

$$\delta_{rb} = -\lambda|\sigma|^J sign(\sigma) + n, \text{ with } J \in \;]0, 0.5] \quad (34)$$

$$\dot{n} = \begin{cases} -b\,sign(\sigma)/(\Omega) & , \text{ if } |\sigma| \leq \Omega \\ -b\,sign(\sigma) & , \text{ if } |\sigma| > \Omega \end{cases}, \quad (35)$$

where Ω is a boundary layer introduced around the sliding surface σ, with $\Omega \in \mathbb{R}^+$ [48].

3) CONVERGENCE AND STABILITY ANALYSIS OF LATERAL FUNCTION

The convergence and stability analysis is necessary to define the parameter values of the higher-order sliding mode controller so that the system converges in a finite time. The second-order sliding algorithm forces σ, $\dot{\sigma}$, and consequently the state variables $(\Delta y, \Delta\dot{y}, \Delta\ddot{y}, \Delta r, \Delta\dot{r})$ to converge to zero at finite time t_r, with t_r defined as the reaching time and bounded to the vehicle initial states. The sufficient conditions to guarantee the convergence is provided by the following approach [47], [71]:

- Consider a dynamic system in the form of

$$\dot{x} = w(t, x) + y(t, x)U, \quad (36)$$

with $w = A[v\ r]^\top$, and $y = B[1\ k]^\top$, from (4).

- The sliding surface derivative $\dot{\Upsilon}$ as

$$\dot{\Upsilon} = E(t, x) + \vartheta(t, x)U. \quad (37)$$

By combining (4), (11) and (13), we have then $\vartheta = -k_r W - \dot{\Phi}$; $E = k_{yd}\Delta\dot{y} + k_{yv}\Delta\ddot{y} + k_r(a_{11}\dot{y} + a_{12}r)$. U as $\delta = \delta_e + \delta_b$, and $W = b_{12} + b_{22}k$.

- Assuming the positive constants Z_u, J, S, q and M satisfies the following constraints [71]

$$\begin{cases} |\dot{E}| + Z_u|\dot{\vartheta}| \leq J \\ 0 \leq S \leq \vartheta(t, x) \leq q \end{cases} \begin{cases} |E/\vartheta| < MZ_U \\ 0 < M < 1, \end{cases} \quad (38)$$

with λ large and $Sb > J$, the controller will force the state variables to converge zero and keep $\Upsilon = \dot{\Upsilon} = 0$. The convergence condition lays on the proper selection of λ and b as

$$\begin{cases} b > J/S \\ \lambda > \sqrt{\dfrac{2}{Sb - J}\dfrac{(Sb + J)q(1 + M)}{S^2(1 - M)}} \end{cases} \quad (39)$$

- The total reaching time t_r defined as [47], [71]

$$t_r \leq \sum|\dot{\sigma}_i|/(Sb - J), \quad (40)$$

with $\dot{\sigma}_i$ the sliding derivative at $\sigma = 0$.

- The controller stability is evaluated by selecting the candidate Lyapunov function as

$$V = \sigma^2/2, \quad \dot{V} = \sigma\dot{\sigma} < 0. \quad (41)$$

From (4), (5), and (6), the lateral acceleration $\dot{v}$ and the yaw acceleration $\dot{r}$ are written as

$$\dot{v} = a_{11}v + a_{12}r + \delta H, \quad (42)$$
$$\dot{r} = a_{21}\dot{v} + a_{22}r + \delta W, \quad (43)$$

where $H = b_{11} + b_{12}/k$. With the vehicle steering angle δ as (12), and substituting (42) and (43) into (41), the Lyapunov function is rewritten as

$$\dot{V} = \sigma Q + (k_{yv}H - k_r\Phi)(\delta_e\sigma - \lambda|\sigma|^2 - b|\sigma|). \quad (44)$$

As $\lambda > 0$, by selecting $|b| > |\delta_e|$, we guarantee the term $(\delta_e\sigma - \lambda|\sigma|^2 - b|\sigma|) < 0$. A sufficient condition for stability is to make the term $(k_{yv}H - k_r\Phi) > 0$. By selecting $(k_{yv}H - k_r\Phi) = 1$, k_{yv} is given in the following form

$$k_{yv} = (1 + k_r\Phi)/H. \quad (45)$$

The Lyapunov stability is guaranteed by making the term $\sigma Q = 0$, with Q written as

$$Q = k_{yd}\Delta\dot{v} + k_{yv}M + k_r r = 0, \quad (46)$$

with

$$M = a_{11}\dot{v} + a_{12}r - \ddot{y}_{ref}. \quad (47)$$

By substituting (45) into (46), the gradient coefficient k_r is given as

$$k_r = -\frac{k_{yd}\Delta\dot{v}H + M}{rH + \Phi M}. \quad (48)$$

Therefore, by selecting b, γ, k_{yv}, and k_r from the proposed approach, we guaranty the system stability with $\dot{V} < 0$. The gradient coefficient k_{yd} is not restricted for the system stability. We select $k_{yd} = 50$.

C. PATH PREVIEW

The path preview technique uses the vehicle's heading angle ϖ and the projected points in front of the vehicle to give the steering controller information about how the car moves relative to the desired path. According to [72], the projection of only one point is insufficient to describe the vehicle's movement over the path. The studies in [60] and [73] applied the multi-point-preview technique to extract the path information. Although it improves compared to a single-point-preview, the path recognition might remain unsatisfactory if the number of projected points is scarce. In this paper, we propose a path preview technique based on look-ahead-areas, as shown in Figure 4. By this approach, all the particularities of the reference path are considered. Along with the vehicle's projection view, we define five different areas A_i ($i = 1, 2, 3, 4, 5$) calculated by
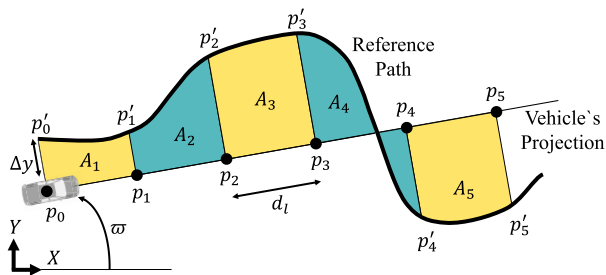
FIGURE 4. Path preview technique with five projected points in front of vehicle and five areas calculated from the vehicle's projection line and the reference path.

$$A_i = \int_{p_{i-1}}^{p_i} f(x)dx, \tag{49}$$

where $f(x)$ is the curvature of the reference path, p_i the projected points that define the areas A_i, and d_l the space between the projected points. Each area receives a gain G_i. The gain defines the significance of each area for the vehicle controller. Higher gain values on the areas far from the vehicle will anticipate lateral movement. Whereas in the area closer to the vehicle it will result in a short noticed movement. The correct choice depends on the desired vehicle behavior. As the current work deals with short time window evasive maneuvering, the gains closer to the vehicle have higher values, i.e.,

$$G_2 = G_3 = G_4 = 1.5, \ G_5 = 0, \tag{50}$$

and

$$G_1 = \begin{cases} 4, & \text{if } u \leq 15 \text{ m/s} \\ 2.2\,u - 29, & \text{if } 15 \text{ m/s} < u \leq 20 \text{ m/s} \\ 15, & \text{if } u > 20 \text{ m/s.} \end{cases} \tag{51}$$

The look-ahead offset o_p, which is the path preview output information given to the steering controller and used in (33), is calculated as

$$o_p = \sum_{i=1}^{n} \frac{G_i A_i}{d_l} + \lambda W_{cg}. \tag{52}$$

A proportional-integral (PI) controller is implemented to force the path difference (Δy) to zero. λ is the PI controller output, calculated as

$$\lambda = K_1 \Delta y(t) + K_2 \int_0^t \Delta y(t)\,dt, \tag{53}$$

where $K_1 = 0.11$, and $K_2 = 0.05$. We define d_l as 6 meters. $W_{cg} = 25$ is the gain associated with λ.

D. LONGITUDINAL CONTROL

The vehicle throttle and brake values Π_j, as shown in Figure 2, are calculated in a four-step process as follows: (i) a longitudinal sliding mode control is designed to determine the optimum throttle and brake values Γ for the vehicle.

(ii) a slip control that monitors the vehicle wheels individually is designed using fuzzy logic and outputs correction values Z_j. (iii) a torque vector is designed with fuzzy logic to distribute the drive and brake torques individually on the vehicle wheels and outputs a correction value X_j. (iv) the final throttle and brake values Π_j are given as

$$\Pi_j = \varrho_j + Z_j * sign(\varrho_j), \text{ with } \Pi, \varrho \in [-1, 1], \tag{54}$$

with ϱ_j defined as

$$\varrho_j = \Gamma + X_j, \text{ with } \Gamma, X \in [-1, 1], \tag{55}$$

in which j is the vehicle wheels such as the front-left fl, front-right fr, the rear-left rl or the rear-right rr. $\Pi_j > 0$ means a throttle request whereas $\Pi_j \leq 0$ means a brake request on the j wheel. The slip control function access the tire slip values. If the tires are close to saturation limits, the slip control reduces the throttle during the acceleration process and the brake value during the braking process. The slip correction values Z_j are in the range of $[-1, 0]$. Therefore, the fuzzy slip control directly impacts (54), while the torque-vectoring fuzzy control directly influences (55). (54) and (55) are the equations responsible for the distribution of the final throttle and brake values Π_j. In next subsections, the pedal value Γ, the slip correction Z, and torque vectoring X values are designed.

E. LONGITUDINAL CONTROL Γ BASED ON SMC

The longitudinal control Γ is designed based on convectional sliding mode control technique. The sliding variable ε is defined as

$$\varepsilon = m_x(\Delta x - D_{des}) + m_a \Delta \dot{x} + m_{yx} \Delta y + m_s \Delta \varphi, \tag{56}$$

where m_x, m_a, m_{yx}, and $m_s \in \mathbb{R}$ are the gradient coefficients. Δx and $\Delta \dot{x}$ are the relative longitudinal distance and relative longitudinal velocity between the ego vehicle and the preceding vehicle. D_{des} is the desired distance between both vehicles, defined as 20 meters. $\Delta \varphi$ is the sum of the monitoring tire factors $S_{r,j}$ on the jth wheel, with $S_{r,j}$ defined in section II-F. The term $m_{yx} \Delta y$ is responsible for the coupling between lateral and longitudinal function, as the lateral path error Δy directly influences the vehicle's longitudinal acceleration. The control law for the desired vehicle acceleration $\Delta \ddot{x}_{soll}$ is defined as [21]

$$\Delta \ddot{x}_{soll} = \begin{cases} \ddot{x}_{max}(\varepsilon/\Psi) & , \text{ for } |\varepsilon| \leq \Psi \\ -sign(\varepsilon)\ddot{x}_{max} & , \text{ for } |\varepsilon| > \Psi, \end{cases} \tag{57}$$

where $\ddot{x}_{max}$ is the absolute maximum permissible acceleration during the emergency maneuvering, and Ψ a boundary layer introduced around the sliding surface [48]. As the goal is to maneuver the vehicle up to handling limits, we choose $\ddot{x}_{max} = 15$ m/s^2. Moreover, we define $\Psi = 5$. A PI controller calculates the optimum throttle and brake pedal value Γ, where the error value $e(t)$ is the difference between the desired acceleration from SMC ($\Delta \ddot{x}_{soll}$), and the actual vehicle longitudinal acceleration x_a (available from the virtual
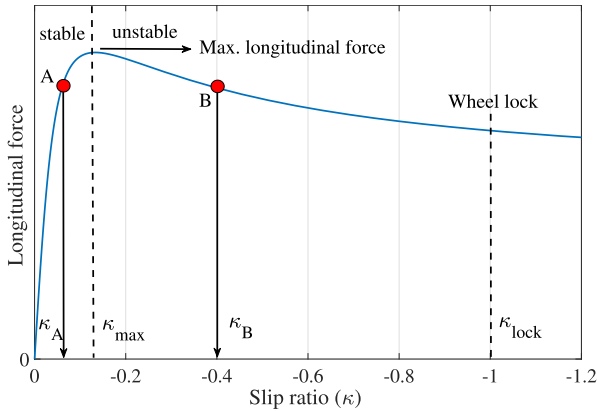
FIGURE 5. Tire saturation monitoring: tire longitudinal force vs. slip ratio with κ_{max} defining the stable and unstable regions.
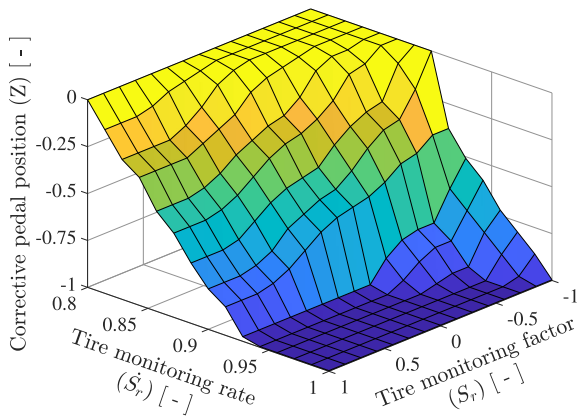

FIGURE 6. Fuzzy slip control surface for front wheels, providing the corrective pedal position value Z in terms of monitoring tire factor S_r and its rate of change $\dot{S}_r$.
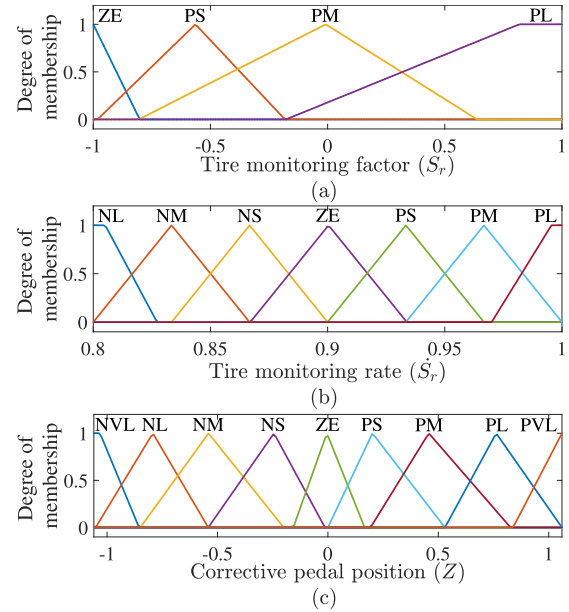

FIGURE 7. Membership functions of the fuzzy slip controller for front wheels regarding (a) monitoring tire factor S_r, (b) its rate of change $\dot{S}_r$, and (c) the corrective pedal position Z.

with

$$\kappa_{x,j} = \frac{\kappa_j}{|\kappa_{max,j}|}, \quad \alpha_{y,j} = \frac{\alpha_j}{|\alpha_{max,j}|}, \qquad (60)$$

where $\kappa_{x,j}$ is the normalized slip ratio on the j wheel, and $\alpha_{y,j}$ the normalized slip angle on the j wheel. $\kappa_{max,j}$ is the longitudinal slip ratio at the maximum tire longitudinal force, as shown in Figure 5. $\alpha_{max,j}$ is the lateral slip at the maximum tire lateral force. S_r, therefore, is the monitoring variable to assess how close the tires are to saturation limits in both longitudinal and lateral directions. In the case κ_A/κ_{max}, the normalized slip ratio $\kappa_{x,j} < 1$, the tire forces are on the stable region. For κ_B/κ_{max}, the normalized slip ratio $\kappa_{x,j} > 1$, the tire has reached the unstable slip region of the tire in the longitudinal direction. The tires locks only when κ_j itself reaches $1(\kappa_{lock})$. Similar interpretation is valid for $\alpha_{y,j}$. Therefore, in the case of $S_r \geq 1$, the tire has reached or exceeded the saturation limits in at least one direction [77].

In this study, we apply slip controllers for each wheel independently. At the front wheels, the slip controllers start correcting the throttle and brake pedals from $S_{r,j} > 0.8$. For the rear wheels, the corrections take place from $S_{r,j} > 0$. The $S_{r,j}$ boundary values were defined during the controller tuning process. This approach is applied to (1) bring the vehicle up to tire saturation limits and (2) keep the vehicle close to saturation limits while performing the maneuver. The slip controller was designed using fuzzy logic [75]. The fuzzy logic theory is selected to design the slip and torque vectoring controllers because it allows the control of non-linear systems, such as the non-linear vehicle behavior, with good performance and robustness [75], [78].

inertial measurement unit). Γ is defined as

$$\Gamma = K_p e(t) + K_{int} \int_0^t e(t)\, dt, \qquad (58)$$

where $K_p = 0.1$ and $K_{int} = 0.5$ are constant gains.

F. SLIP CONTROL DESIGN Z_j

Slip control is used in the vehicle to prevent skidding and to maximize tire forces, thereby contributing to the vehicle's stability [74]. A common approach is to design a controller that corrects the throttle and brake pedals immediately when slip occurs [74], [75]. The tire is characterized by the lateral slip α and the longitudinal slip ratio κ (see [58], [76]). The tire workload on the jth wheel can be monitored by the tire forces or tire slip values. According to Joa et al. [77], force-based tire saturation monitoring is unsuitable for practical application at the handling limits, first because it is harder to estimate than slip values, second because of the slip-force curve convex shape. The monitoring tire factor $S_{r,j}$ of the jth wheel is defined in dimensionless term as

$$S_{r,j} = \sqrt{\kappa_{x,j}^2 + \alpha_{y,j}^2}, \qquad (59)$$

The fuzzy controller rules rely on the tire factor S_r and its rate of change $\dot{S}_r$. Since S_r is dimensionless, $\dot{S}_r$ is also dimensionless. $\dot{S}_r$ can be interpreted as how fast the lateral and longitudinal slips α and κ are approaching the saturation limits. The slip control surface and membership functions are similar for front and rear wheels, only differing in the S_r range, i.e., front wheels from 0.8 to 1 and rear wheels from 0 to 1. The slip control surface for the front wheels is shown in Figure 6. The corrective pedal position Z is the slip controller output. Z ranges from 0 to -1, e.g., if full throttle is requested on the front left wheel ($\varrho_{fl} = 1$) and Z outputs the value -1, no throttle is applied to the electric motors ($\Pi_{fl} = 0$ as in (54)). On the other hand, if full brake is requested on the front left wheel ($\varrho_{fl} = -1$) and Z outputs the value -1, no brake is applied ($\Pi_{fl} = 0$ as in (54)). The membership functions are shown in Figure 7. The control rule is based on [75].

G. TORQUE VECTORING DESIGN X_j

Torque vectoring (TV) is an active vehicle dynamics control system that can apply torque on each wheel to create a corrective yaw moment M_{zTV}. The corrective yaw moment via TV is generated by manipulating brake and drive actuators, which is fully practicable in the case of 4WID and 4WD vehicles. Torque vectoring increases the vehicle's cornering response and, consequently, vehicle safety [79]. The total vehicle's yaw moment M_{zveh} and the corrective yaw moment M_{zTV} requested by torque vectoring are defined as [80]

$$M_{zk} = M_{zk,front} + M_{zk,rear} = \Theta_{front}M_{zk} + \Theta_{rear}M_{zk}, \quad (61)$$

where $k = TV$ for the requested yaw moment via the TV, and $k = veh$ for the total vehicle's yaw moment. Θ_{front} and Θ_{rear} are the percentage of the required moment in the front and rear wheels. The relation between Θ_{front} and Θ_{rear} defines the front-to-rear moment distribution, with $\Theta_{rear} = 1 - \Theta_{front}$.

In this work, we apply the torque vectoring using fuzzy control proposed by Li et al. [81], with the advantage that we consider not only the braking torque, but we also include driving torque to generate the corrective moment M_{zTV}. The control surface for the yaw moment M_{zTV} is shown in Figure 8 in dimensionless (dl) terms as M_{zTVdl}. Δr is the difference between desired and actual yaw rate, and $\Delta\beta$ is the difference between desired and actual side slip angle, with the desired side slip angle $\beta_d = v_{ref}/u$, and the desired yaw rate defined in (11). The yaw moment M_{zTVdl} is depicted from $+1$ to -1, with positive values representing a required yaw moment in the anti-clockwise direction and negative values a required yaw moment in the clockwise direction, with Figure 3 as reference. Therefore, the requested yaw moment M_{zTV} is generated by individually manipulating each vehicle wheel's brake and motor actuators. The maximum driving torque generated on each wheel is limited by the electric motor's maximum torque, T_{emax}. The maximum brake torque is limited to T_{bmax}. T_{emax} and T_{bmax} values are defined in section III.

The front-to-rear moment distribution Θ_{front} is calculated by a fuzzy controller, with the control surface shown in
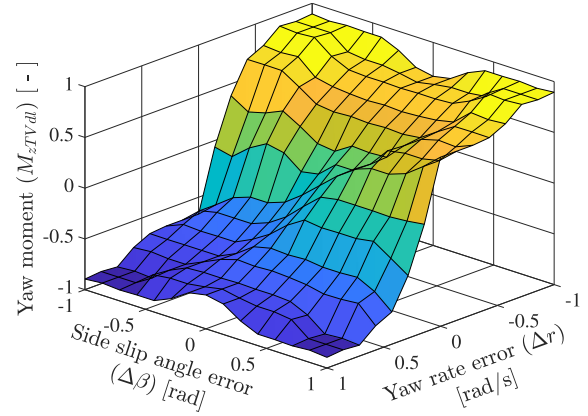

FIGURE 8. Control surface for the yaw moment M_z in terms of side slip angle error $\Delta\beta$, and the yaw rate error Δr.
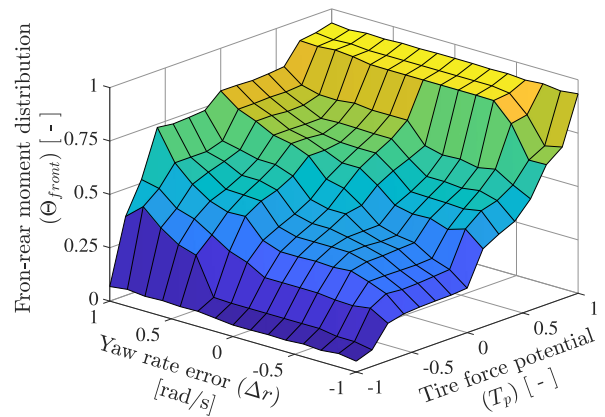

FIGURE 9. Control surface for the front-to-rear moment distribution Θ_{front} in terms of the yaw rate error Δr, and tire force potential T_p.

Figure 9. Θ_{front} is depicted from 0 to 1, with 1 representing that 100% of the yaw moment is generated in the front wheels and 0% at the rear wheels. The inputs of the fuzzy controller are the yaw rate error Δr and the tire force potential T_p, defined as

$$T_p = \left(1 - \frac{S_{r,fl} + S_{r,fr}}{2}\right) - \left(1 - \frac{S_{r,rl} + S_{r,rr}}{2}\right), \quad (62)$$

with $T_p \in [-1,1]$, and $S_{r,i} \in [0,1]$. The tire force potential T_p provides information on the remaining potential of the tires on the front and rear axle to resist lateral and longitudinal forces. $T_p = 1$ means that both rear tires reached unstable tire slip, while the front tires are on stable region with $\kappa_{fl} = \kappa_{fr} = 0$, and $\alpha_{fl} = \alpha_{fr} = 0$. $T_p = -1$ has the opposite meaning. The membership functions are shown in Figure 10. The control rule base is shown in table 1 [81]. The correction value X_j is calculated as

$$X_j = \begin{cases} cM_{zTVdl}\Theta_{front} \\ cM_{zTVdl}\Theta_{rear}, \end{cases} \quad (63)$$
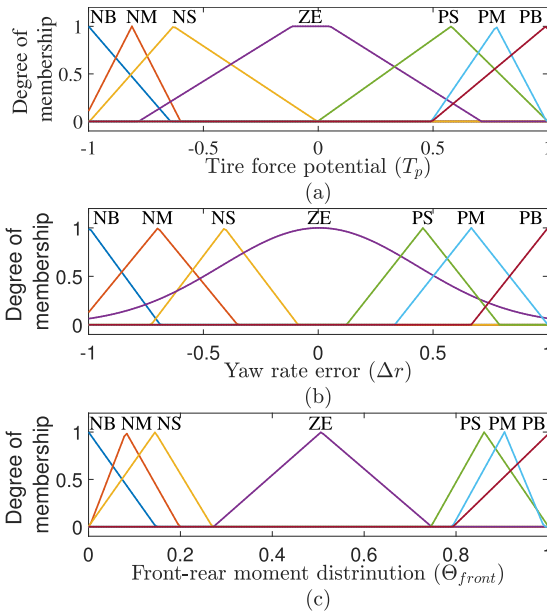
FIGURE 10. Membership functions of (c) the fuzzy front-rear moment distribution controller Θ_{front} regarding (a) the difference between desired and actual yaw rate Δr, and (b) the tire force potential T_p.

TABLE 1. Control rules for fuzzy front-rear moment distribution Θ_{front}.

$T_p/\Delta r$	PB	PM	PS	ZE	NS	NM	NB
PB	PB	PB	PB	PB	PB	PB	PB
PM	PM	PB	PM	PM	PM	PS	PS
PS	PM	PM	PM	PS	PS	PS	ZE
ZE	PS	PS	PS	ZE	NS	NS	NS
NS	PS	ZE	NS	NS	NS	NM	NM
NM	NS	NS	NS	NM	NM	NB	NB
NB	NB	NB	NB	NB	NB	NB	NB

with $c = -1$ for fl and rl wheels, and $c = 1$ for fr and rr wheels. The total vehicle's yaw moment M_z is calculated as

$$M_{zveh} = \frac{T_w}{r_{eff}}\{-T_{fl}sign(\Pi_{fl}) + T_{fr}sign(\Pi_{fr})$$
$$- T_{rl}sign(\Pi_{rl}) + T_{rr}sign(\Pi_{rr})\} \quad (64)$$

with $T_{fl}, T_{fr}, T_{rl}, T_{rr}$ as the individual wheel torques, and r_{eff} the tire effective rolling radius. The requested yaw moment via torque vectoring (M_{zTV}) is calculated as a function of X_j and ϱ_j as

$$M_{zTV} = \frac{T_w}{r_{eff}} \sum_{n=4}^{j} \begin{cases} X_j T_{emax}, \text{ if } \varrho_j \geq 0 \\ -X_j T_{bmax}, \text{ if } \varrho_j < 0, \end{cases} \quad (65)$$

III. VEHICLE SIMULATION SOFTWARE

We test the vehicle controller in IPG CarMaker® by using a high-fidelity Renault Megane vehicle model, with the main vehicle properties shown in table 2. We model the vehicle powertrain as electric 4WID, the vehicle steering system as 4WIS, and the brake system as 4WIB. The brakes are a conventional brake system with dynamic behavior modeled

TABLE 2. Vehicle properties.

Property	m_v	l_f	l_r	T_w	I_z	r_{eff}
Value	1250	1.041	1.628	1.591	1848.7	0.305
Unit	kg	m	m	m	kgm²	m

as [82]

$$\frac{T_{act}}{T_{cal}} = \frac{e^{-T_d s}}{T_a s + 1}, \quad (66)$$

where T_{act} is the applied brake torque on the wheels, T_{cal} is theoretical brake torque before considering the dynamic brake effect, and it is calculated as

$$T_{cal} = \Pi_j * T_{bmax}, \quad (67)$$

with T_{bmax} the maximum brake torque on the j wheel. $T_{bmax} = 1800$ Nm for front wheels and $T_{bmax} = 1200$ Nm for rear wheels. Based on [19] and [83] we define $T_d = 0.06$, and $T_a = 0.12$ for front wheels, and $T_d = 0.02$, and $T_a = 0.05$ for rear wheels. The dynamic behavior of the electric motors is modeled considering a linear relationship between the throttle pedal and the motor driving torque, as in [84]. The maximum electric motor torque $T_{emax} = 185$ Nm and the maximum brake torque T_{bmax} are provided in the IPG CarMaker® vehicle model catalogs.

IV. TEST SCENARIOS AND PERFORMANCE INDICATORS

We evaluate the proposed evasive maneuvering controller in a critical scenario. Up to date, no standard tests are available to evaluate combined lateral and longitudinal functions in evasive maneuverings [19]. We define a critical scenario that consists of a single lane-change maneuver, similar to [19]. The ego vehicle travels at a constant speed when a preceding vehicle is detected at a distance D_{det} of 30 meters, as shown in Figure 11. The preceding vehicle is in standing still condition. We propose an emergency steering combined with emergency braking. Once the object is detected, the controller performs the lane change and simultaneously applies brakes, and brings the vehicle to a stand-still position. We choose this condition because it is challenging for vehicle controllers to handle nonlinearities in the lateral and longitudinal directions simultaneously. The lane width L_w is set to 3.0 meters. We assume that the adjacent lane is free, without incoming or outgoing vehicles.

Assessment metrics are necessary to evaluate the effectiveness of automated driving systems. Safety metrics include, e.g., time-to-collision (TTC) and time-to-brake (TTB). TTC and TTB are among the most used safety metrics in critical situations [85], [86], [87]. The benefits of TTC include its formulation simplicity and effectiveness for rear-end scenarios. The main disadvantage of TTC relies on scenarios in which vehicles move with zero relative velocity or scenarios with lateral collisions [85]. The TTB is often combined with TTC to evaluate if the vehicle can avoid a crash by only applying brakes. Therefore, since this study deals with rear-end collision, no lateral crashes, and relative longitudinal velocities
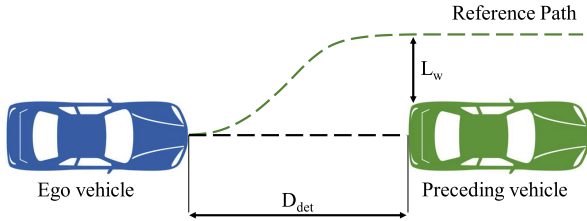
FIGURE 11. Critical scenario: single lane-change maneuver with ego vehicle detecting the preceding vehicle with a distance of D_{det}, and lane width L_w.

TABLE 3. Varying ego vehicle longitudinal velocity u.

μ_a [-]	u [km/h]						
1.0	75	80	90	100	110	120	130

TABLE 4. Varying road friction μ_a.

u [km/h]	μ_a [-]					
80	0.5	0.6	0.7	0.8	0.9	1.0

greater than zero, TTC and TTB are sufficient safety metrics to evaluate the vehicle controller, as in [19]. TTC and TTB are defined as

$$TTC = \frac{D_{det}}{u}; \; TTB = \frac{u}{2a_{max}}, \quad (68)$$

where a_{max} is the maximum acceleration, assumed as $\mu_a g$. μ_a is the road adhesion friction coefficient, and g is the gravitational acceleration. Evasive maneuvering is necessary if TTB is greater than TTC, meaning that a full brake in a straight line is not enough to avoid a crash and a steering maneuver is necessary. The reference path design takes place by using a Sigmoidal membership function [88]

$$y_{ref} = \frac{L_w}{1 - e^{-a(x-C)}}, \quad (69)$$

where x is the vehicle longitudinal position, a the Sigmoid curve slope, and C is a tuning parameter to define the length of the lane change. We defined $a = 5$ and $C = 15$. We evaluate the controller performance and robustness by using a variety of scenario conditions as follows.

A. VARYING EGO LONGITUDINAL VELOCITY
In the first test set, we vary the longitudinal vehicle velocity from 75 km/h to 130 km/h, keeping the road friction constant at 1.0. Table 3 outlines the scenarios.

B. VARYING ROAD FRICTION μ_a
In the second set, we keep the velocity constant at 80 km/h and vary the road friction from 0.5 to 1.0, as in table 4.

C. PERFORMANCE INDICATORS
We assess the vehicle controller performance by addressing four performance indicators (PI). The first performance indicator is the distance to collision (DTC), representing the
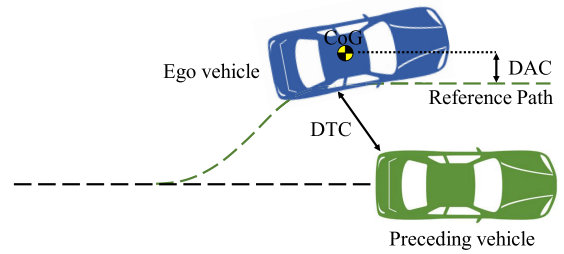
FIGURE 12. Graphical representation of the distance to collision (DTC) and the distance to adjacent center lane (DAC).

minimum distance between the ego vehicle's outer shell and the preceding vehicle's outer shell. The second PI is the distance between the ego vehicle CoG and the adjacent center lane (DAC). Both DTC and DAC are depicted in Figure 12. The last PIs are the maximum lateral and longitudinal accelerations.

The DTC is the main parameter for collision avoidance since it identifies how close the ego vehicle is to a collision and if it occurs. DTC should be as high as possible, meaning that the ego vehicle does not collide with the preceding vehicle and can keep a safe distance. DTC = 0 means that a collision occurred. As the lane change maneuver is combined with steering and braking, the ego vehicle might come to a halt for low initial velocities even before reaching the adjacent lane, resulting in a DAC with negative values. DAC = 0 means that the ego vehicle came to a halt with its CoG lying exactly above the centerline of the adjacent lane. DAC is of great interest for higher velocities, where the vehicle crosses the centerline of the adjacent center lane before reaching the standstill position. In this case, DAC should be small as possible, meaning that the vehicle does not exceed the road limits. High accelerations mean that the controller managed to bring the vehicle to the handling limits while still successfully performing the evasive lane change.

D. CONSTRAINTS
We implement constraints to approximate the proposed design to a practical vehicle controller application. These constraints are:

- Controller sampling time of 100 Hz to emulate the real functionality of a vehicle electronic unit control (ECU).
- Maximum steering angle ratio of $\pm 960°/s$.
- Maximum steering angle $\pm 20°$.

V. SIMULATION RESULTS
The vehicle controller was tested for the scenarios described in section IV. In this section, the results are explained first by presenting the lane-change situation at 130 km/h and later presenting the results for different road frictions.

A. VARYING VELOCITY
Figure 13 shows the ego vehicle behavior for an emergency lane change at 130 km/h. When the ego vehicle was at
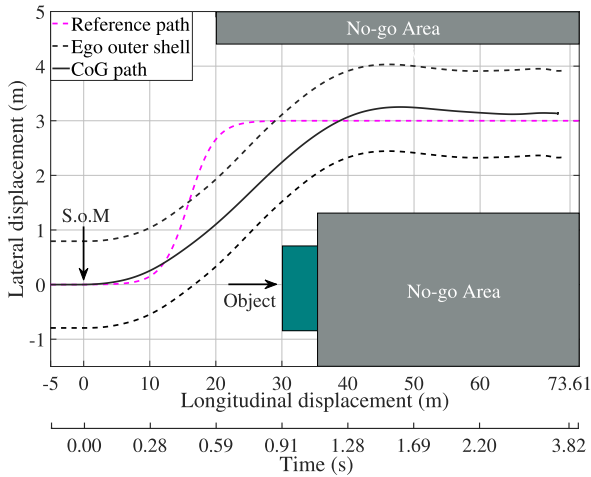
FIGURE 13. Ego vehicle behaviour during single lane-change emergency maneuver with initial velocity of 130 km/h.


FIGURE 14. (a) Steering angles for each wheel, and (b) vehicle longitudinal velocity for emergency maneuver with initial velocity of 130 km/h.


FIGURE 15. Desired and actual yaw rate during emergency maneuver with initial velocity of 130 km/h.

position 0 meters, the controller received the information that a preceding vehicle (object) was 30 meters ahead. Based on the environment information and vehicle properties, the controller then calculated TTC and TTB. As the TTB was higher than TTC, meaning that braking only would not be enough to avoid a crash, the controller acknowledged the need for an emergency lane change. A reference path with 3 meters width was generated assuming no traffic in the adjacent lane, as shown in the dashed pink line in Figure 13. The start-of-maneuver (S.o.M) took place at 0 meters. The green box (labeled as object) shows the boundaries of the preceding vehicle. The no-go areas represent the area in front of the object and, on the top, the limits of the road. The solid black line in Figure 13 represents the center-of-gravity trajectory of the ego vehicle, with the ego vehicle's outer shell displayed as dashed black lines. The minimum distance to the collision was 0.42 meters. In less than 1.3 seconds, the vehicle reached the adjacent lane with an overshoot of 0.273 meters (9.1%). Afterward, the controller kept the vehicle on track by following the straight part of the reference path. Therefore, the controller successfully handled the vehicle in an emergency lane change at 130 km/h while avoiding the collision with the preceding vehicle and keeping the vehicle within the road boundaries. The controller in [19] performed a lane change with continuous driving instead of simultaneous braking, as proposed in this study. Although the vehicle desired velocity after detection differs, a comparison to [19] can identify our controller's advantages. In [19], the lane change was performed in 1.7 seconds at 90 km/h, with a lane width of 2.5 meters. The maximum velocity that the controller handled an evasive maneuver was 100 km/h. Therefore, our controller shows a clear benefit since it successfully avoids crashes up to 130 km/h and performs a lance change in less than 1.3 seconds. Moreover, since our scenario's lane width was 3.0 meters, the vehicle had an extra 0.5 meters to move in the lateral direction, which is more challenging than shorter lane widths.
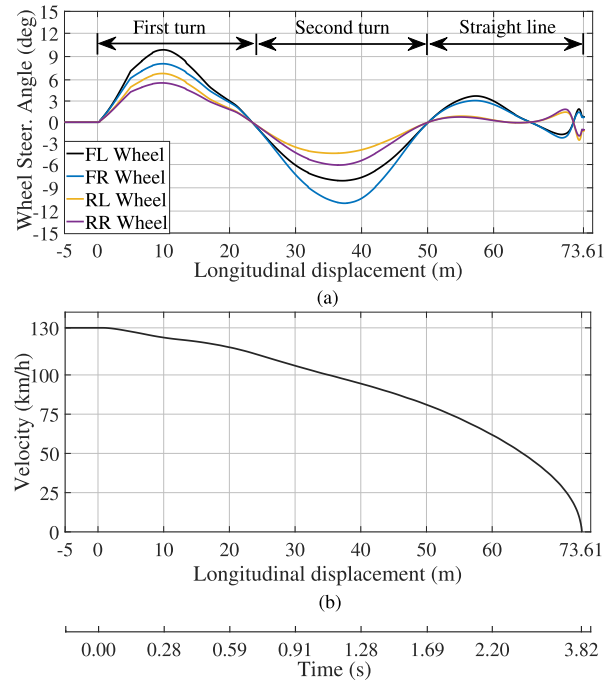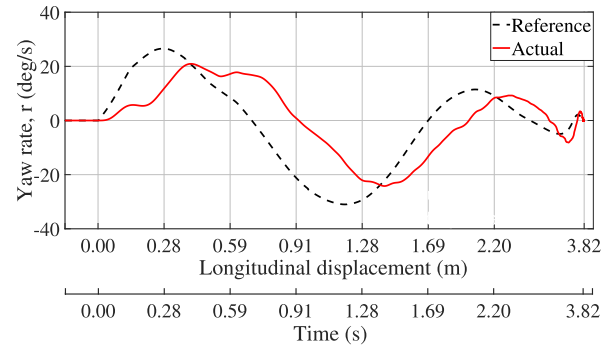
Figures 14 and 15 illustrate the steering values for each wheel, longitudinal velocity, and yaw rates. The single-lane change was initiated with a left turn, followed by a right turn, and then a straight-line driving with minor correction on the steering. From the beginning of the maneuver until around 0.14 seconds, the steering angles showed a linear response because they reached the maximum values for steering angle ratio. The front and rear axles steer in the same direction between 130 km/h and 50 km/h. In contrast, they have opposite directions below 50 km/h, with the steering ratio calculated from (9) as a function of vehicle velocity.

From the beginning of the lane change, the controller actuated the steering and the brakes simultaneously, which can be observed by comparing the steering angles and the brake torques on each wheel, which is shown in Figure 16.
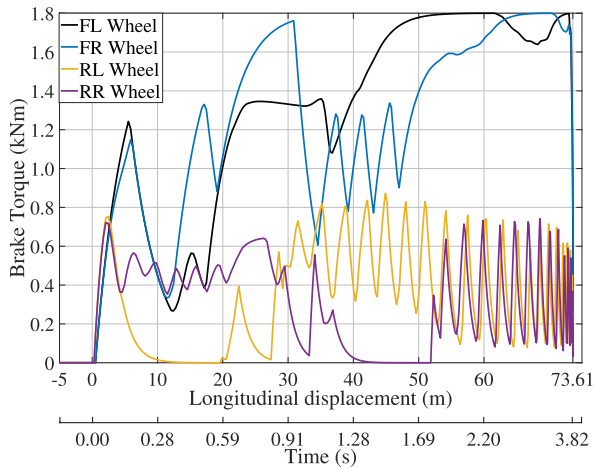
FIGURE 16. Brake torque on the vehicle wheels during single lane-change emergency maneuver with initial velocity of 130 km/h.
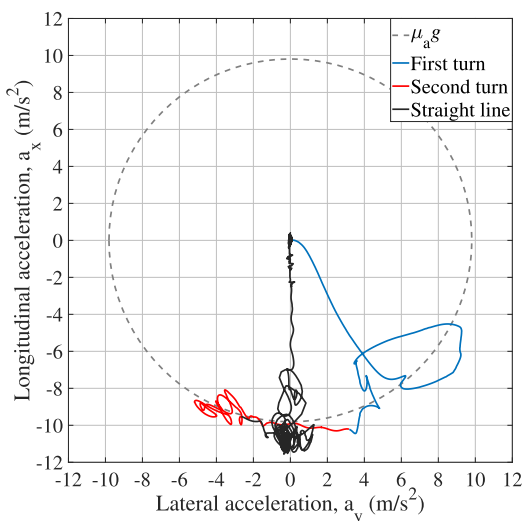

FIGURE 17. Acceleration g-g diagram during single lane-change emergency maneuver with initial velocity of 130 km/h.

At the detection point (0 meters), the vehicle started the steering process and the brake actuation. The velocity is reduced from 130 km/h to around 100 km/h when the ego-vehicle starts overtaking the preceding vehicle (at the position of 30 meters). During the whole maneuver process, it is observed that the controller applies the brakes on the four wheels independently to bring the vehicle to a standstill. The ego vehicle was brought to a complete stop after 3.82 seconds the object was detected, with a total longitudinal displacement of 73.61 meters. In [19], the maximum brake torque values reached 105 Nm during the lane change and 800 Nm in straight-line braking. As our controller applied simultaneous lane change with full braking request, the braking torque reached up to 1250 Nm in the first turn and up to 1720 Nm in the second turn as shown in Figure 16, proving the successful actuation of lateral and longitudinal motion to keep the vehicle on track while braking.

The ego vehicle's longitudinal and lateral accelerations are shown in Figure 17 (g-g diagram). The blue line depicts the accelerations in the first curve, the red line in the second curve, and the black line in the straight-line driving. The grey circle represents the acceleration limits for the adhesion friction coefficient (μ_a). The total friction coefficient (μ) results from the interaction between the adhesion (μ_a) and the deformation term (μ_d), with $\mu = \mu_a + \mu_d$. The adhesion term μ_a occurs in the real contact area between the tire and the road, which in the investigated scenario is equal to 1.0. The deformation term μ_d arises from viscoelastic damping properties of the tire [89]. The maximum possible friction value depends on the tire properties, road characteristics, vehicle, and wheel dynamics. For dry asphalt, the maximum friction value occurs for slip angles around 0.2 radians, with a μ value close to 1.2 [90]. For the selected tire model (MF52 205/60R15 91V [58]), the maximum friction value μ is 1.18. Therefore, the vehicle accelerations can reach values beyond the adhesion friction limits ($\mu_a g$) and below 1.18 g, as shown in Figure 17.

The vehicle experienced high lateral and longitudinal accelerations from the beginning of the evasive maneuvering due to the simultaneous steering and braking actuation. In the middle of the first turn, the lateral acceleration reached a value of 9.24 m/s², and simultaneously the longitudinal acceleration reached −4.78 m/s². The vehicle controller applied the brakes to bring the vehicle to a standstill while steering to keep the vehicle on track. The acceleration values are most of the time at the limits of the adhesion circle, with extrapolation of the adhesion limits occurring at some moments. During the second turn, the lateral accelerations stay between −5.2 m/s² to −3 m/s² for 0.62 seconds. When the vehicle was close to finishing the lane change and keeping the straight line, the controller increased the brake torques and used most of the tire's potential in the longitudinal direction. The straight line section started at 1.69 seconds and lasted until the end of the maneuver, at 3.82 seconds (as seen in Figure 14). During this period, the controller kept the longitudinal accelerations from −9.9 m/s² up to −11.4 m/s² until the end of the maneuver, which is favorable for emergency braking situations. The evasive maneuver in [19] reached a maximum of 6 m/s² in the lateral direction and 0.5 m/s² in the longitudinal direction, thus below the adhesion limits. Therefore, our controller shows superiority since it handles the vehicle beyond the adhesion limits, e.g., the vehicle accelerations up to 8.7 m/s² in the lateral direction while reaching up to −7.5 m/s² during the first turn. While our controller handles the vehicle in an extremely aggressive driving zone for the entire maneuver, the controller in [19] only reached extreme aggressiveness in the lateral direction for a limited time, with aggressiveness driving acceleration ranges defined in [28].

In Figure 18, the normalized slip saturation circle for each wheel is shown. The normalized slip angle $\alpha_{y,j}$ is shown in the horizontal direction, while the vertical direction shows the normalized slip ratio $\kappa_{y,j}$ (equation (60)). During the first turn,
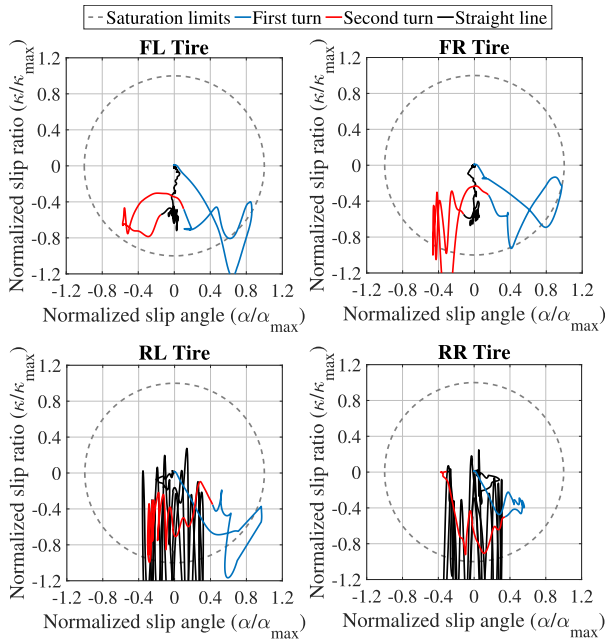
FIGURE 18. Normalised slip ratios and normalised slip angles during single lane-change emergency maneuveliner with initial velocity of 130 km/h.

FIGURE 19. Vertical loads on the wheels during single lane-change emergency maneuver with initial velocity of 130 km/h.

three of four wheels exceed the saturation limits. Although the normalized slip ratio and angle reached values beyond saturation, the controller bring back the longitudinal and lateral slips inside the saturation circle. Ideally, the optimum normalized slip value during the evasive maneuvering is 1.0, meaning that the controller can use the maximum possible tire forces on each wheel during the maneuver without overpassing to the unstable tire slip region. As depicted in Figure 18, the controller attempted to use the maximum tire forces by adjusting steering and brake to keep the normalized slip values close to the saturation limits. The normalized slip ratio and angle were kept inside the saturation limits for three of four tires during the second turn. The front right tire exceeded the saturation values for less than 100 ms. When the ego vehicle was close to finalizing the lane change and keeping the straight path (black line in Figure 18), most of the vehicle load was transferred to the front wheels due to the brake actuation, as observed in Figure 19. Consequently, while the controller attempted to brake using the maximum longitudinal forces on each rear wheel, the brake actuation became sensitive to additional torque. Thereby both brake torques and slip ratio on the rear tires presented an oscillating effect, as depicted by Figures 16, 18, and 19.

Figure 19 presents the vertical load on each tire during the emergency maneuvering. In the first 100 ms of the first turn, the vertical load on both rear tires decreased due to brake actuation with the vehicle still driving in an almost straight line. From 100 ms, there was a load transfer from left to right tires due to the first turning movement. The load on the rear-left tire reached 0 N from 0.17 s to 0.5 s, meaning a loss of contact with the ground for more than 300 ms. This
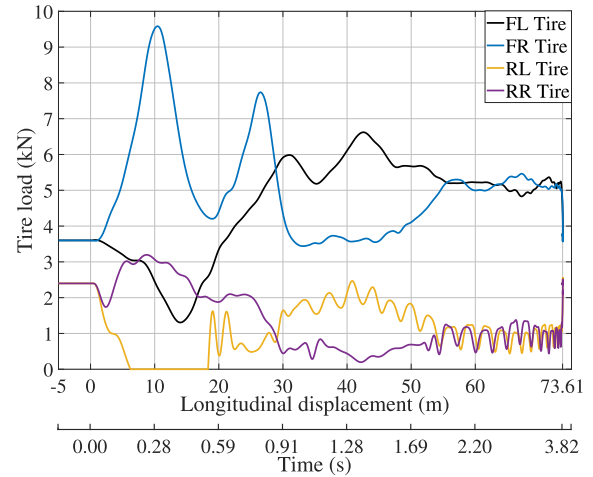
phenomenon shows that the controller managed to handle the vehicle under extreme conditions where one of the tires is not in contact with the ground. During the second turn, with the vehicle turning to the right, the load transfer occurred from right to left. During the straight-line section, the load on both front tires was similar and higher than the rear tires due to brake actuation.

For the emergency maneuver described in Section IV, the controller generated the corrective yaw moment M_z via the vehicle's independent brake actuation and did not apply the electric drive. For other driving scenarios, such as lane-change followed by continuous driving as in [19], the controller generates M_z by actuating brakes and electric drive. However, such a scenario is outside the framework of this paper.

Figure 20 shows the total vehicle's yaw moment, the requested yaw moment by the TV controller, and the yaw moment generated by the TV controller. At the start of the maneuver, the TV controller requests a positive yaw moment to support the vehicle movement when the steering wheel angles have a positive rate of increase, as depicted in Figure 14. During the first turn, for a negative steering angle rate, the required yaw moment reduces and turns into a negative value in an attempt to support the vehicle to rotate in a clockwise direction. Note that, although the controller requested in the first turn up to 4200 Nm, a maximum of 2100 Nm was generated via TV on the wheels, as depicted in Figure 20 (a). The difference between the requested and generated yaw moment is due to: (1) the torques on the wheels can not extrapolate the maximum brake torque T_{bmax} nor the maximum drive torque T_{emax}. (2) the slip controller adjusts the throttle and brake pedals to keep the vehicle near the saturation limits, as shown in Figure 18. Therefore, the maximum permissible throttle and brake torques are limited by their theoretical maximum values and by the slip controller. For instance, since the rear-right wheel keeps within the saturation limits during the first turn, as depicted in Figure 18,

the TV controller generates a yaw moment by adjusting the brake request on the *rr* wheel. As the steering wheel angle decreases during the first turn and the requested yaw moment becomes negative, no yaw moment is generated via TV on the *rr* wheels since it would extrapolate the maximum permissible brake torque. The TV controller similarly adjusts the wheel torques on the *fl*, *fr*, and *rl* wheels. The individual yaw moment and generated wheel torques for the individual wheels are depicted in Figure 21. Since during most of the first turn the *fl*, *fr*, and *rl* wheels reach the saturation limits, the TV controller ceases to manipulate these wheels while the slip controller attempts to adjust the throttle and brake pedals to keep within the saturation limits. Most of the yaw moment delivered via TV are on the left wheels during the second turn. The TV controller generates torque on *fl* and *rl* by manipulating the brake pedals while requesting brake torque on the right wheels beyond the brake limits T_{bmax}. Therefore, no extra torque is generated via TV on the right wheels at the end of the first and for most of the second turns. Note that the requested torques via the TV controller show abrupt changes due to the influence of the slip controller. The TV request signals are computed to the final throttle and brake values Π_j, and only then is the signal passed to either the dynamic brake behavior or the electric drive behavior. e.g., in Figure 21 the generated torques on the wheels show abrupt changes, while the brake torque on the wheels behaves based on the dynamic brake model and shows a smother behavior as in Figure 16. At the end of the maneuver, with the vehicle in an almost straight line, the delivered torque via the TV controller oscillates since the wheels are in and out of the saturation limits, as depicted in Figure 18.

The distance-to-collision (DTC) is presented in Figure 22 for the varying velocity scenarios. At 130km/h, the vehicle successfully avoided the collision with a safe margin of 0.42 meters. As the velocity of the ego vehicle decreases, the DTC increases, thus increasing the safe margins. The distance to the adjacent center lane (DAC) is another important factor that shows the safety of the evasive lane change. Ideally, the vehicle can not exceed the road limits when performing the lane change. A positive and non-zero DAC value means an overshoot with the ego vehicle crossing the centerline of the adjacent lane, which occurred for velocities above 100 km/h. The maximum overshoot distance was 0.273 m at 130 km/h. For a safe lane change, the maximum overshoot value should be in the range of 0.5 to 0.75 meters for lane width from 3 to 3.5 meters, respectfully [39]. Therefore, the proposed controller successfully performed the evasive lane change for all the velocities within the safe margins without crashing into the preceding vehicle or extrapolating the road boundaries. A negative DAC means that the ego vehicle reached a standstill position while not even crossing the centerline of the adjacent lane, which occurred for velocities below 110 km/h.

Figure 23 shows the longitudinal braking distance concerning the vehicle velocity at the start of the evasive maneuvering. Braking distances ranged from 73.61 meters
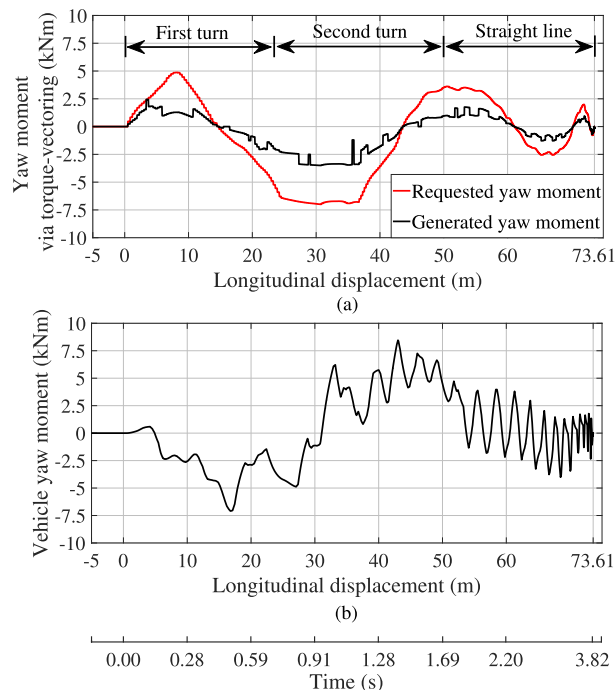

FIGURE 20. (a) Requested M_{zTV} and generated yaw moment via torque-vectoring, and (b) total vehicle yaw moment M_z.
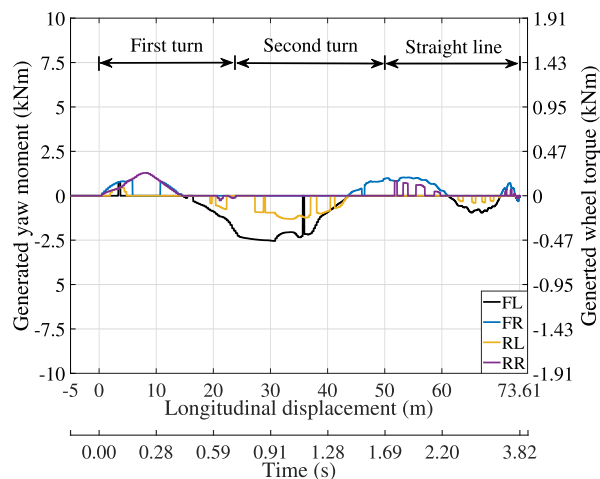

FIGURE 21. Generated yaw moment and generated wheel torque in individual vehicle's wheels.

at 130 km/h to 34.2 meters at 75 km/h, representing an improvement in the braking performance compared to state-of-the-art emergency braking controllers with a reduction in the total braking distance. The maximum longitudinal deceleration and lateral accelerations related to the initial vehicle velocity are shown in Figure 23. For all cases, the maximum deceleration values tend to increase with the longitudinal velocity and were above -10.6 m/s². Similarly, the lateral acceleration tends to increase with velocity, with values ranging from 7.5 m/s² at 75 km/h, to 11.3 m/s² at 130 km/h. The observed values show that the proposed controller brings the ego vehicle to the handling limits for all the test cases.
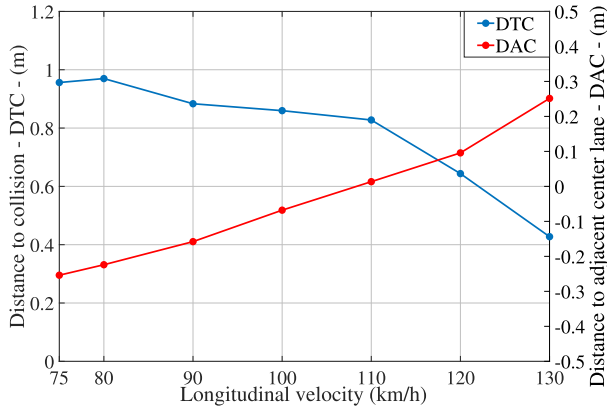
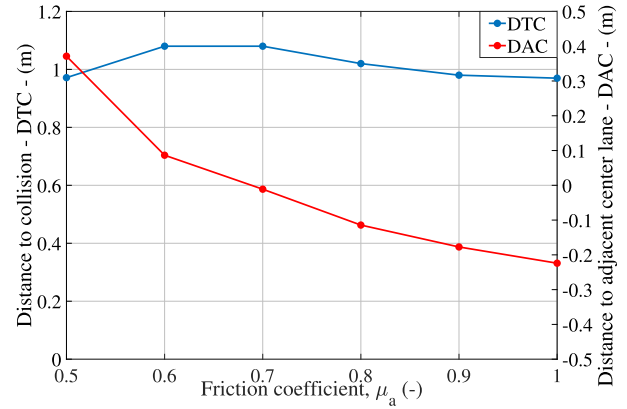**FIGURE 22.** Distance to collision (DTC) and distance to adjacent center lane (DAC) by varying ego velocity scenarios.

FIGURE 24. Distance to collision (DTC) and distance to adjacent center lane (DAC) by varying road friction scenario.
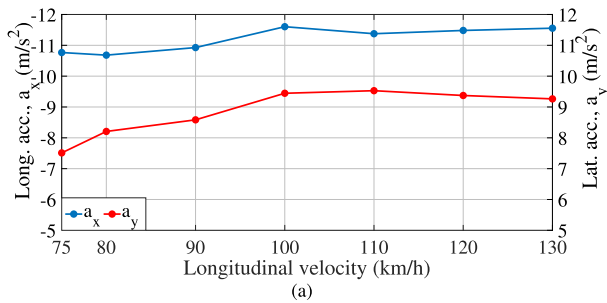

FIGURE 23. (a) Maximum accelerations in m/s², and (b) and braking distance by varying ego velocity scenarios.

FIGURE 25. (a) Maximum longitudinal and lateral accelerations in m/s², and (b) braking distance by varying road friction scenarios.

B. VARYING ROAD FRICTION

The vehicle controller was tested by varying the road friction μ_a from 0.5 to 1.0 with the ego velocity of 80 km/h at the object detection point. As shown in Figure 24, decreasing the friction coefficient keeps the distance to collision around 1 meter. It demonstrates that the vehicle controller is also capable of keeping safe distances with low friction coefficients. For $\mu_a \geq 0.7$, the ego vehicle came to a halt before reaching the adjacent lane's centerline. For $\mu_a < 0.7$, the ego vehicle crossed the adjacent center lane before a complete stop, with an overshoot within the safety margins and below 0.4 meters.

As expected, the braking distance increases with a decrease in the road friction, as shown in Figure 25. Because the vehicle controller attempted to use the maximum brake forces during the maneuver, the longitudinal accelerations were kept at the limits, reaching a maximum deceleration of 6.2 m/s² for

$\mu_a = 0.5$, and a braking distance of fewer than 60 meters for this case. The maximum longitudinal and lateral acceleration decreased with reduced road friction due to the reduction of the maximum lateral and longitudinal tire forces. Nevertheless, the controller managed to reach the vehicle handling limits for all tested cases and avoid the crash successfully.

VI. CONCLUSION

We have developed a coupled lateral and longitudinal vehicle controller in this paper. The controller aims to maneuver the ego vehicle under critical situations within a short time window to crash. The longitudinal and lateral parts of the controller are developed using the sliding mode control theory. The coupling between both parts is accomplished by introducing a lateral sliding mode equation as a function of the longitudinal velocity and proposing a longitudinal sliding equation in terms of the lateral vehicle velocity. The tire slip saturation is taken into account on the sliding equation of the

lateral controller and therefore influences the vehicle steering request directly. On the longitudinal part, a torque vectoring fuzzy controller distributes the brake and the acceleration request between the vehicle's wheels and adjusts the vehicle yaw moment during the evasive maneuver. The fuzzy slip control adjusts the brake and the throttle pedals to keep the tires close to the saturation limits.

We evaluated the controller in a simulation environment in scenarios that considered different vehicle velocities up to 130km/h at the detection point and different road frictions. The controller effectively handles the vehicle to perform the lane change for all the scenarios while simultaneously steering and applying the brakes to bring the vehicle to a complete stop. The collision is avoided in all cases, with the vehicle kept inside the road boundaries. The controller brings the vehicle to its handling limits and experiences high lateral and longitudinal accelerations. The controller's purpose is to bring the vehicle to a safe position where safety is more important than comfort while avoiding a crash. Therefore, comfort driving is not considered a constraint for the controller.

The simulated test vehicle was equipped with front and rear steering. This setup and the proposed controller allow for crash avoidance at high velocities and 30 meters from the proceeding object. Therefore, this work assists in investigating the benefits of new vehicle controllers for emergency maneuvering with front and rear steering configurations. The controller is tested with a 10 ms frequency to emulate real embedded systems, thus making the simulation practical.

REFERENCES

[1] J. Nieuwenhuijsen, G. H. D. A. Correia, D. Milakis, B. van Arem, and E. van Daalen, "Towards a quantitative method to analyze the long-term innovation diffusion of automated vehicles technology using system dynamics," *Transp. Res. C, Emerg. Technol.*, vol. 86, pp. 300–327, Jan. 2018, doi: 10.1016/j.trc.2017.11.016.

[2] C.-Y. Chan, "Advancements, prospects, and impacts of automated driving systems," *Int. J. Transp. Sci. Technol.*, vol. 6, no. 3, pp. 208–216, 2017, doi: 10.1016/j.ijtst.2017.07.008.

[3] J. Funke, M. Brown, S. M. Erlien, and J. C. Gerdes, "Collision avoidance and stabilization for autonomous vehicles in emergency scenarios," *IEEE Trans. Control Syst. Technol.*, vol. 25, no. 4, pp. 1204–1216, Jul. 2017, doi: 10.1109/TCST.2016.2599783.

[4] E. Jeong, C. Oh, and S. Lee, "Is vehicle automation enough to prevent crashes? Role of traffic operations in automated driving environments for traffic safety," *Accident Anal. Prevention*, vol. 104, pp. 115–124, Jul. 2017, doi: 10.1016/j.aap.2017.05.002.

[5] A. Eskandarian, *Handbook of Intelligent Vehicles*. London, U.K.: Springer, 2012, doi: 10.1007/978-0-85729-085-4.

[6] W. Yang, J. Liu, K. Zhou, Z. Zhang, and X. Qu, "An automatic emergency braking model considering driver's intention recognition of the front vehicle," *J. Adv. Transp.*, vol. 2020, pp. 1–15, Dec. 2020, doi: 10.1155/2020/5172305.

[7] J. Souman, "Human factors guidelines report 2: Driver support systems overview," TNO, Helmond, The Netherlands, Tech. Rep. TNO 2020 R12167, 2021.

[8] A. Seewald, C. Haß, M. Keller, and T. Bertram, "Emergency steering assist for collision avoidance," *ATZ Worldwide*, vol. 117, no. 1, pp. 14–19, Jan. 2015, doi: 10.1007/s38311-015-0147-1.

[9] Y.-M. Lin and B.-C. Chen, "Handling enhancement of autonomous emergency steering for reduced road friction using steering and differential braking," *Appl. Sci.*, vol. 11, no. 11, p. 4891, May 2021, doi: 10.3390/app11114891.

[10] C. Qian, "A homogeneous domination approach for global output feedback stabilization of a class of nonlinear systems," in *Proc. Amer. Control Conf.*, Portland, OR, USA, 2005, pp. 4708–4715, doi: 10.1109/ACC.2005.1470739.

[11] Q. Meng, C. Qian, Z.-Y. Sun, and C.-C. Chen, "A homogeneous domination output feedback control method for active suspension of intelligent electric vehicle," *Nonlinear Dyn.*, vol. 103, no. 2, pp. 1627–1644, Jan. 2021, doi: 10.1007/s11071-020-06188-z.

[12] Q. Meng, Z. Sun, Z. Shen, and H. He, "Homogeneous domination-based lane-keeping control method for intelligent vehicle," *Nonlinear Dyn.*, vol. 111, no. 7, pp. 6349–6362, Apr. 2023, doi: 10.1007/s11071-022-08159-y.

[13] Q. Meng, Z.-Y. Sun, Y. Shu, and T. Liu, "Lateral motion stability control of electric vehicle via sampled-data state feedback by almost disturbance decoupling," *Int. J. Control*, vol. 92, no. 4, pp. 734–744, Aug. 2019, doi: 10.1080/00207179.2017.1367104.

[14] Q. Meng, H. Xu, and Z.-Y. Sun, "Nonlinear lateral motion stability control method for electric vehicle based on the combination of dual extended state observer and domination approach via sampled-data output feedback," *Trans. Inst. Meas. Control*, vol. 43, no. 10, pp. 2258–2271, Jun. 2021, doi: 10.1177/0142331221994369.

[15] Q. Meng, C. Qian, and P. Wang, "Lateral motion stability control via sampled-data output feedback of a high-speed electric vehicle driven by four in-wheel motors," *J. Dyn. Syst., Meas., Control*, vol. 140, no. 1, Jan. 2018, doi: 10.1115/1.4037266.

[16] G. Zhang, Q. Wang, T. Mujumdar, and T. Sugiarto, "Path planning and motion control in evasive steering assist," SAE, Warrendale, PA, USA, Tech. Paper nos. 2022-01-0088, 2022, doi: 10.4271/2022-01-0088.

[17] T. Bächle, K. Graichen, M. Buchholz, and K. Dietmayer, "Vehicle dynamics control in challenging driving situations using nonlinear model predictive control allocation," in *Proc. IEEE Conf. Control Appl. (CCA)*, Juan Les Antibes, France, Oct. 2014, pp. 346–351, doi: 10.1109/CCA.2014.6981370.

[18] G. Devineau, P. Polack, F. Altché, and F. Moutarde, "Coupled longitudinal and lateral control of a vehicle using deep learning," in *Proc. 21st Int. Conf. Intell. Transp. Syst. (ITSC)*, Maui, HI, USA, Nov. 2018, pp. 642–649, doi: 10.1109/ITSC.2018.8570020.

[19] N. Chowdhri, L. Ferranti, F. S. Iribarren, and B. Shyrokau, "Integrated nonlinear model predictive control for automated driving," *Control Eng. Pract.*, vol. 106, Jan. 2021, Art. no. 104654, doi: 10.1016/j.conengprac.2020.104654.

[20] R. Hajiloo, M. Abroshan, A. Khajepour, A. Kasaiezadeh, and S. K. Chen, "Integrated steering and differential braking for emergency collision avoidance in autonomous vehicles," *IEEE Trans. Intell. Transp. Syst.*, vol. 22, no. 5, pp. 3167–3178, May 2021, doi: 10.1109/TITS.2020.2984210.

[21] T. Eigel, "Integrierte längs- und Querführung von personenkraftwagen mittels sliding-mode-regelung," Ph.D. Thesis, TU Braunschweig, Logos-Verlag, Braunschweig, Germany, 2010, doi: 10.24355/dbbs.084-201007071617-0.

[22] R. Chen, Z. Chen, Y. Duan, J. Wu, and Y. Zhang, "Coupled longitudinal and lateral control for trajectory tracking of autonomous vehicle based on LTV-MPC approach," SAE, Warrendale, PA, USA, Tech. Paper nos. 2022-01-0296, 2022, doi: 10.4271/2022-01-0296.

[23] L. Ge, Y. Zhao, F. Ma, and K. Guo, "Towards longitudinal and lateral coupling control of autonomous vehicles using offset free MPC," *Control Eng. Pract.*, vol. 121, Apr. 2022, Art. no. 105074, doi: 10.1016/j.conengprac.2022.105074.

[24] C. Kim, Y. Yoon, S. Kim, M. J. Yoo, and K. Yi, "Trajectory planning and control of autonomous vehicles for static vehicle avoidance in dynamic traffic environments," *IEEE Access*, vol. 11, pp. 5772–5788, 2023, doi: 10.1109/ACCESS.2023.3236816.

[25] X. Wang, D. Wang, M. Du, K. Song, Y. Ni, and Y. Li, "A two-layer trajectory tracking control scheme of manipulator based on ELM-SMC for autonomous robotic vehicle," *IEEE Trans. Autom. Sci. Eng.*, early access, Jan. 24, 2023, doi: 10.1109/TASE.2023.3238349.

[26] A. Chebly, R. Talj, and A. Charara, "Coupled longitudinal/lateral controllers for autonomous vehicles navigation, with experimental validation," *Control Eng. Pract.*, vol. 88, pp. 79–96, Jul. 2019, doi: 10.1016/j.conengprac.2019.05.001.

[27] Y. Xie, "Coupled fractional-order sliding mode control and obstacle avoidance of a four-wheeled steerable mobile robot," *ISA Trans.*, vol. 108, pp. 282–294, Feb. 2021, doi: 10.1016/j.isatra.2020.08.025.

[28] I. Bae, J. Moon, and J. Seo, "Toward a comfortable driving experience for a self-driving shuttle bus," *Electronics*, vol. 8, no. 9, p. 943, Aug. 2019, doi: 10.3390/electronics8090943.

[29] C. M. Martínez and D. Cao, "2—Integrated energy management for electrified vehicles," in *Ihorizon-Enabled Energy Management for Electrified Vehicles*, C. M. Martínez and D. Cao, Eds. Oxford, U.K.: Butterworth-Heinemann, 2019, pp. 15–75, doi: 10.1016/B978-0-12-815010-8.00002-8.

[30] M. Van, S. S. Ge, and H. Ren, "Robust fault-tolerant control for a class of second-order nonlinear systems using an adaptive third-order sliding mode control," *IEEE Trans. Syst., Man, Cybern. Syst.*, vol. 47, no. 2, pp. 221–228, Feb. 2016, doi: 10.1109/TSMC.2016.2557220.

[31] S. Ding, C. Huang, C. Ding, and X. Wei, "Straight-line tracking controller design of agricultural tractors based on third-order sliding mode," *Comput. Electr. Eng.*, vol. 106, Mar. 2023, Art. no. 108559, doi: 10.1016/j.compeleceng.2022.108559.

[32] J. Liu, L. Gao, J. Zhang, and F. Yan, "Super-twisting algorithm second-order sliding mode control for collision avoidance system based on active front steering and direct yaw moment control," *Proc. Inst. Mech. Engineers, D, J. Automobile Eng.*, vol. 235, no. 1, pp. 43–54, Jan. 2021, doi: 10.1177/0954407020948298.

[33] Y. Yu and X. Liu, "Model-free fractional-order sliding mode control of electric drive system based on nonlinear disturbance observer," *Fractal Fractional*, vol. 6, no. 10, p. 603, Oct. 2022, doi: 10.3390/fractalfract6100603.

[34] N. S. Özbek, "Design and real-time implementation of a robust fractional second-order sliding mode control for an electromechanical system comprising uncertainties and disturbances," *Eng. Sci. Technol., Int. J.*, vol. 35, Nov. 2022, Art. no. 101212, doi: 10.1016/j.jestch.2022.101212.

[35] K. Hu, X. Chen, L. Weng, L. Tian, and Y. Hu, "A survey of deep neural network sliding mode control in robot application," in *Proc. Chin. Autom. Congr. (CAC)*, Shanghai, China, 2020, pp. 6659–6662, doi: 10.1109/CAC51589.2020.9327212.

[36] J. Tan, Y. Fan, P. Yan, C. Wang, and H. Feng, "Sliding mode fault tolerant control for unmanned aerial vehicle with sensor and actuator faults," *Sensors*, vol. 19, no. 3, p. 643, Feb. 2019, doi: 10.3390/s19030643.

[37] L. El Hajjami, E. M. Mellouli, V. Žuraulis, M. Berrada, and I. Boumhidi, "A robust intelligent controller for autonomous ground vehicle longitudinal dynamics," *Appl. Sci.*, vol. 13, no. 1, p. 501, Dec. 2022, doi: 10.3390/app13010501.

[38] X. Du and K. Kiong Tan, "Autonomous vehicle velocity and steering control through nonlinear model predictive control scheme," in *Proc. IEEE Transp. Electrific. Conf. Expo, Asia–Pacific (ITEC Asia–Pacific)*, Busan, South Korea, Jun. 2016, pp. 1–6, doi: 10.1109/ITEC-AP.2016.7513089.

[39] S. Milani, H. Khayyam, H. Marzbani, W. Melek, N. L. Azad, and R. N. Jazar, "Smart autodriver algorithm for real-time autonomous vehicle trajectory control," *IEEE Trans. Intell. Transp. Syst.*, vol. 23, no. 3, pp. 1984–1995, Mar. 2022, doi: 10.1109/TITS.2020.3030236.

[40] J. Edrén, "Motion modelling and control strategies of over-actuated vehicles," Ph.D. Thesis, Dept. Vehicle Eng., Königliche Technische Hochschule (KTH), Stockholm, 2014.

[41] P. Hang and X. Chen, "Towards autonomous driving: Review and perspectives on configuration and control of four-wheel independent drive/steering electric vehicles," *Actuators*, vol. 10, no. 8, p. 184, Aug. 2021, doi: 10.3390/act10080184.

[42] S. Yim, "Comparison among active front, front independent, 4-wheel and 4-wheel independent steering systems for vehicle stability control," *Electronics*, vol. 9, no. 5, p. 798, May 2020, doi: 10.3390/electronics9050798.

[43] Q. Meng, Z.-Y. Sun, and Y. Li, "Finite-time controller design for four-wheel-steering of electric vehicle driven by four in-wheel motors," *Int. J. Control, Autom. Syst.*, vol. 16, no. 4, pp. 1814–1823, Aug. 2018, doi: 10.1007/s12555-017-0509-0.

[44] B. Shyrokau, D. Wang, D. Savitski, K. Hoepping, and V. Ivanov, "Vehicle motion control with subsystem prioritization," *Mechatronics*, vol. 30, pp. 297–315, Sep. 2015, doi: 10.1016/j.mechatronics.2014.11.004.

[45] *BMVI—Federal Ministry for Digital and Transport—Germany will be the World Leader in Autonomous Driving*, Accessed: Nov. 24, 2022. [Online]. Available: https://www.bmvi.de/SharedDocs/EN/Articles/DG/act-on-autonomous-driving.html

[46] M. Steinberger, M. Horn, and L. Fridman, *Variable-Structure Systems and Sliding-Mode Control*, vol. 271. Cham, Switzerland: Springer, 2020, doi: 10.1007/978-3-030-36621-6.

[47] Y. Shtessel, C. Edwards, L. Fridman, and A. Levant, *Sliding Mode Control and Observation*. New York, NY, USA: Springer, 2014, doi: 10.1007/978-0-8176-4893-0.

[48] C. Edwards and S. K. Spurgeon, *Sliding Mode Control*, vol. 1. London, U.K.: CRC Press, 1998, doi: 10.1201/9781498701822.

[49] I. Boiko, L. Fridman, A. Pisano, and E. Usai, "Analysis of chattering in systems with second-order sliding modes," *IEEE Trans. Autom. Control*, vol. 52, no. 11, pp. 2085–2102, Nov. 2007, doi: 10.1109/TAC.2007.908319.

[50] H. Benariba and A. Boumediene, "Lateral sliding mode control of an electric vehicle," in *Proc. 6th Int. Conf. Control Eng. Inf. Technol. (CEIT)*, Istanbul, Turkey, Oct. 2018, pp. 1–5, doi: 10.1109/CEIT.2018.8751932.

[51] G. Tagne, R. Talj, and A. Charara, "Higher-order sliding mode control for lateral dynamics of autonomous vehicles, with experimental validation," in *Proc. IEEE Intell. Vehicles Symp. (IV)*, Gold Coast, QLD, Australia, Jun. 2013, pp. 678–683, doi: 10.1109/IVS.2013.6629545.

[52] L. Tan, S. Yu, Y. Guo, and H. Chen, "Sliding-mode control of four wheel steering systems," in *Proc. IEEE Int. Conf. Mechatronics Autom. (ICMA)*, Takamatsu, Japan, Aug. 2017, pp. 1250–1255, doi: 10.1109/ICMA.2017.8015996.

[53] A. Mehta and B. Bandyopadhyay, *Emerging Trends in Sliding Mode Control*, vol. 318. Singapore: Springer, 2021, doi: 10.1007/978-981-15-8613-2.

[54] A. Manzanilla, E. Ibarra, S. Salazar, Á. E. Zamora, R. Lozano, and F. Muñoz, "Super-twisting integral sliding mode control for trajectory tracking of an unmanned underwater vehicle," *Ocean Eng.*, vol. 234, Aug. 2021, Art. no. 109164, doi: 10.1016/j.oceaneng.2021.109164.

[55] H. Zheng and S. Yang, "A trajectory tracking control strategy of 4WIS/4WID electric vehicle with adaptation of driving conditions," *Appl. Sci.*, vol. 9, no. 1, p. 168, Jan. 2019, doi: 10.3390/app9010168.

[56] P. Hang, X. Xia, and X. Chen, "Handling stability advancement with 4WS and DYC coordinated control: A gain-scheduled robust control approach," *IEEE Trans. Veh. Technol.*, vol. 70, no. 4, pp. 3164–3174, Apr. 2021, doi: 10.1109/TVT.2021.3065106.

[57] S. Sano, Y. Furukawa, and S. Shiraishi, "Four wheel steering system with rear wheel steer angle controlled as a function of steering wheel angle," SAE, Warrendale, PA, USA, Tech. Paper 860625, 1986, doi: 10.4271/860625.

[58] H. B. Pacejka, *Tire and Vehicle Dynamics*. Oxford, U.K.: Butterworth-Heinemann, 2012, doi: 10.1016/C2010-0-68548-8.

[59] C. Yin, S. Wang, X. Li, G. Yuan, and C. Jiang, "Trajectory tracking based on adaptive sliding mode control for agricultural tractor," *IEEE Access*, vol. 8, pp. 113021–113029, 2020, doi: 10.1109/ACCESS.2020.3002814.

[60] K. Jalali, S. Lambert, and J. McPhee, "Development of a path-following and a speed control driver model for an electric vehicle," *SAE Int. J. Passenger Cars Electron. Electr. Syst.*, vol. 5, no. 1, pp. 100–113, Apr. 2012, doi: 10.4271/2012-01-0250.

[61] U. Ozguner, K. A. Unyelioglu, and C. Hatipoglu, "An analytical study of vehicle steering control," in *Proc. Int. Conf. Control Appl.*, Albany, NY, USA, Sep. 1995, pp. 125–130, doi: 10.1109/CCA.1995.555653.

[62] A. J. Tremlett, F. Assadian, D. J. Purdy, N. Vaughan, A. P. Moore, and M. Halley, "Quasi-steady-state linearisation of the racing vehicle acceleration envelope: A limited slip differential example," *Vehicle Syst. Dyn.*, vol. 52, no. 11, pp. 1416–1442, Nov. 2014, doi: 10.1080/00423114.2014.943927.

[63] M. Veneri and M. Massaro, "A free-trajectory quasi-steady-state optimal-control method for minimum lap-time of race vehicles," *Vehicle Syst. Dyn.*, vol. 58, no. 6, pp. 933–954, Jun. 2020, doi: 10.1080/00423114.2019.1608364.

[64] D. L. Brayshaw and M. F. Harrison, "A quasi steady state approach to race car lap simulation in order to understand the effects of racing line and centre of gravity location," *Proc. Inst. Mech. Eng., D, J. Automobile Eng.*, vol. 219, no. 6, pp. 725–739, Jun. 2005, doi: 10.1243/095440705X11211.

[65] M. Klomp, "Longitudinal force distribution and road vehicle handling," Ph.D. Thesis, Dept. Appl. Mech., Chalmers Univ. Technol., Gothenburg, Sweden, 2010.

[66] B. Siegler, A. Deakin, and D. Crolla, "Lap time simulation: Comparison of steady state, quasi- static and transient racing car cornering strategies," SAE, Warrendale, PA, USA, Tech. Paper 2000-01-3563, 2000, doi: 10.4271/2000-01-3563.

[67] X. Li, N. Xu, K. Guo, and Y. Huang, "An adaptive SMC controller for EVs with four IWMs handling and stability enhancement based on a stability index," *Vehicle Syst. Dyn.*, vol. 59, no. 10, pp. 1509–1532, Oct. 2021, doi: 10.1080/00423114.2020.1767795.

[68] A. E. M. Ahmed and M. Zohdy, "Sliding mode control for singularly perturbed systems using accurate reduced model," *Int. J. Modern Nonlinear Theory Appl.*, vol. 10, no. 1, pp. 1–12, 2021, doi: 10.4236/ijmnta.2021.101001.

[69] K. R. Prasad, P. D. Reddy, M. B. Chakkravaarthy, and K. K. Ankam, "An adaptive sliding mode controller for high power factor boost rectifier in continuous conduction mode," *Int. J. Comput. Appl.*, vol. 41, no. 14, pp. 45–49, Mar. 2012, doi: 10.5120/5613-7889.

[70] H. Yu and U. Ozguner, "Adaptive seeking sliding mode control," in *Proc. Amer. Control Conf.*, Minneapolis, MN, USA, Jun. 2006, p. 6, doi: 10.1109/ACC.2006.1657462.

[71] A. Levant, "Sliding order and sliding accuracy in sliding mode control," *Int. J. Control*, vol. 58, no. 6, pp. 1247–1263, Dec. 1993, doi: 10.1080/00207179308923053.

[72] R. S. Sharp, D. Casanova, and P. Symonds, "A mathematical model for driver steering control, with design, tuning and performance results," *Veh. Syst. Dyn.*, vol. 33, no. 5, pp. 289–326, 2000, doi: 10.1076/0042-3114(200005)33:5;1-Q;FT289.

[73] X. Ji, Y. Liu, X. He, K. Yang, X. Na, C. Lv, and Y. Liu, "Interactive control paradigm-based robust lateral stability controller design for autonomous automobile path tracking with uncertain disturbance: A dynamic game approach," *IEEE Trans. Veh. Technol.*, vol. 67, no. 8, pp. 6906–6920, Aug. 2018, doi: 10.1109/TVT.2018.2834381.

[74] J. H. Park and C. Y. Kim, "Wheel slip control in traction control system for vehicle stability," *Veh. Syst. Dyn.*, vol. 31, no. 4, pp. 263–278, 1999, doi: 10.1076/vesd.31.4.263.4232.

[75] K. Jalali, T. Uchida, J. McPhee, and S. Lambert, "Development of a fuzzy slip control system for electric vehicles with in-wheel motors," *SAE Int. J. Alternative Powertrains*, vol. 1, no. 1, pp. 46–64, Apr. 2012, doi: 10.4271/2012-01-0248.

[76] J. P. Pauwelussen, *Essentials of Vehicle Dynamics*. Oxford, U.K.: Butterworth-Heinemann, 2015, doi: 10.1016/C2014-0-00503-5.

[77] E. Joa, K. Park, Y. Koh, K. Yi, and K. Kim, "A tyre slip-based integrated chassis control of front/rear traction distribution and four-wheel independent brake from moderate driving to limit handling," *Vehicle Syst. Dyn.*, vol. 56, no. 4, pp. 579–603, Apr. 2018, doi: 10.1080/00423114.2017.1397276.

[78] B. L. Boada, M. J. L. Boada, and V. Díaz, "Fuzzy-logic applied to yaw moment control for vehicle stability," *Veh. Syst. Dyn.*, vol. 43, no. 10, pp. 753–770, 2005, doi: 10.1080/00423110500128984.

[79] C. Chatzikomis, M. Zanchetta, P. Gruber, A. Sorniotti, B. Modic, T. Motaln, L. Blagotinsek, and G. Gotovac, "An energy-efficient torque-vectoring algorithm for electric vehicles with multiple motors," *Mech. Syst. Signal Process.*, vol. 128, pp. 655–673, Aug. 2019, doi: 10.1016/j.ymssp.2019.03.012.

[80] K. Jalali, T. Uchida, S. Lambert, and J. McPhee, "Development of an advanced torque vectoring control system for an electric vehicle with in-wheel motors using soft computing techniques," *SAE Int. J. Alternative Powertrains*, vol. 2, no. 2, pp. 261–278, Apr. 2013, doi: 10.4271/2013-01-0698.

[81] B. Li, D. Li, and F. Yu, "Vehicle yaw stability control using the fuzzy-logic controller," in *Proc. IEEE Int. Conf. Veh. Electron. Saf.*, Beijing, Dec. 2007, pp. 1–5, doi: 10.1109/ICVES.2007.4456392.

[82] J. Zhou, J. Lu, and H. Peng, "Vehicle stabilisation in response to exogenous impulsive disturbances to the vehicle body," *Int. J. Vehicle Auto. Syst.*, vol. 8, nos. 2-3-4, p. 242, 2010, doi: 10.1504/IJVAS.2010.035798.

[83] S. Kuutti, R. Bowden, H. Joshi, R. de Temple, and S. Fallah, "End-to-end reinforcement learning for autonomous longitudinal control using advantage actor critic with temporal context," in *Proc. IEEE Intell. Transp. Syst. Conf. (ITSC)*, Auckland, New Zealand, Oct. 2019, pp. 2456–2462, doi: 10.1109/ITSC.2019.8917387.

[84] J. Hu, C. Sun, J. Xiao, and J. Li, "A torque compensation strategy in two-speed automated mechanical transmission shift process for pure electric vehicles," *Adv. Mech. Eng.*, vol. 7, no. 11, Nov. 2015, Art. no. 168781401561691, doi: 10.1177/1687814015616915.

[85] D. Nalic, T. Mihalj, F. Orucevic, M. Schabauer, C. Lex, W. Sinz, and A. Eichberger, "Criticality assessment method for automated driving systems by introducing fictive vehicles and variable criticality thresholds," *Sensors*, vol. 22, no. 22, p. 8780, Nov. 2022, doi: 10.3390/s22228780.

[86] J. Wishart, S. Como, M. Elli, B. Russo, J. Weast, N. Altekar, E. James, and Y. Chen, "Driving safety performance assessment metrics for ADS-equipped vehicles," *SAE Int. J. Adv. Current Practices Mobility*, vol. 2, no. 5, pp. 2881–2899, Apr. 2020, doi: 10.4271/2020-01-1206.

[87] L. Westhofen, C. Neurohr, T. Koopmann, M. Butz, B. Schütt, F. Utesch, B. Neurohr, C. Gutenkunst, and E. Böde, "Criticality metrics for automated driving: A review and suitability analysis of the state of the art," *Arch. Comput. Methods Eng.*, vol. 30, no. 1, pp. 1–35, Jan. 2023, doi: 10.1007/s11831-022-09788-7.

[88] L. Iliadis, S. Skopianos, S. Tachos, and S. Spartalis, "A fuzzy inference system using Gaussian distribution curves for forest fire risk estimation," in *Artificial Intelligence Applications and Innovations*, H. Papadopoulos, A. S. Andreou, and M. Bramer, Eds. Berlin, Germany: Springer, 2010, pp. 376–386, doi: 10.1007/978-3-642-16239-8_49.

[89] M. Salehi, J. W. M. Noordermeer, L. A. E. M. Reuvekamp, W. K. Dierkes, and A. Blume, "Measuring rubber friction using a laboratory abrasion tester (LAT100) to predict car tire dry ABS braking," *Tribology Int.*, vol. 131, pp. 191–199, Mar. 2019, doi: 10.1016/j.triboint.2018.10.011.

[90] R. Hoseinnezhad and A. Bab-Hadiashar, "Efficient antilock braking by direct maximization of tire–road frictions," *IEEE Trans. Ind. Electron.*, vol. 58, no. 8, pp. 3593–3600, Aug. 2011, doi: 10.1109/TIE.2010.2081951.

AMAURI DA SILVA JUNIOR received the Diploma degree in automotive engineering from the Federal University of Santa Catarina, Brazil. He is currently pursuing the Ph.D. degree with RMIT University, Melbourne, Australia. His research interests include vehicle control for autonomous vehicles and emergency maneuvering controllers.

CHRISTIAN BIRKNER received the master's and Ph.D. degrees in mechanical engineering from the Technical University of Kaiserslautern, in 1990 and 1994, respectively. He is currently a Professor of vehicle systems and controls with Technische Hochschule Ingolstadt, Germany.

REZA NAKHAIE JAZAR received the master's degree in robotics from Tehran Polytechnic, in 1990, and the Ph.D. degree in nonlinear dynamics and applied mathematics from the Sharif University of Technology, in 1997. He is currently a Professor in mechanical engineering with RMIT University.

HORMOZ MARZBANI received the Ph.D. degree in mechanical engineering from RMIT University, Melbourne, Australia, in 2015. Since 2015, he has been a Lecturer with RMIT University. His research interests include dynamics, vibration, vehicle dynamics, and autonomous vehicles.

● ● ●